NUMERICAL AND EXPERIMENTAL INVESTIGATIONS IN THE INSTABILITY AND BREAKUP OF CAPILLARY WATER JETS

by

Nima Moallemi

B.Sc. in Mechanical Engineering, Shahid Bahonar University of Kerman, Iran, 2006
M.Sc. in Mechanical Engineering, Iran University of Science and Technology, Iran, 2009

A THESIS SUBMITTED IN PARTIAL FULFILLMENT OF
THE REQUIREMENTS FOR THE DEGREE OF

MASTER OF APPLIED SCIENCE

in

THE COLLEGE OF GRADUATE STUDIES

(Mechanical Engineering)

THE UNIVERSITY OF BRITISH COLUMBIA

(Okanagan)

June 2014

Abstract

In this thesis, the instability and breakup of free capillary jets are investigated. Both numerical and experimental methodologies are used to define the breakup process for capillary jets. High speed photography is used to capture droplet formation and to measure breakup length. In parallel, numerical simulations based on the volume of fluid (VOF) approach, with interface tracking and adaptive meshing are performed to provide further insight into the jet instabilities. The VOF method enables accurate tracking of the interface while reducing computational cost by means of adaptive grids. The growth rate of disturbance is compared with the theoretical prediction from a dispersion relation obtained by first-order perturbation analysis. Moreover, the numerical results show a good agreement with experimental data for the breakup length of the liquid jet under different wave numbers. The velocity profile and the pressure gradient in the necking zone of the jet are analyzed to clarify the droplet detachment process. In addition, Lagrangian analysis of fluid particles in the jet shows that when droplet detachment occurs, the direction of fluid particles changes dramatically due to droplet oscillations.

Keywords: Jet Instability, Multiphase Flow, High Speed Photography, Volume of Fluid, Breakup Length

Table of Contents

List of Tables:

List of Figures:

Acknowledgements

Firstly I would like to thank my supervisors Dr. Li and Dr. Mehravaran for all of their help and support. Their advice and valuable guidance have been invaluable in the completion of my thesis, and without their assistance, this project would have not been possible.

It is an honor for me to have Dr. Joshua Brinkerhoff and Dr. Kenneth Chau as my internal advisory committee members and Dr. Boris Stoeber for their encouraging words, feedback and advice on thesis, and time and attention during busy semesters.

I would also like to thank my friends and family for their continued support and assistance. I am deeply grateful to my sister, Negin, for being supportive and caring sister. I am always proud of you.

Finally, I owe my deepest gratitude to my wife, Sadaf for her unconditional love and support that means everything for me.

Dedication

To my family who supported me each step of the way.

List of Symbols

a	Orifice radius
c	Volume fraction function
D	Orifice diameter
E	Voltage
f	Frequency
H	Curvature
I_0 , I_1, I_m	Bessel functions
k	Spatial wavenumber
K_m	Modified Bessel functions
L	Breakup length
L_o	Unperturbed jet breakup length
m	Azimuthal wavenumber
M	Viscosity ratio
p	Pressure
R	Jet radius
R_1 , R_2	Curvature radius
t	Time
t_0	Initial time
U	Jet velocity
U_0	Mean jet velocity
U_*	Projection velocity
V	Radial velocity
V_0	Dripping velocity
V_c	Critical velocity
x	Axial coordinate
$\bar{x}$	Moving frame of axial coordinate
β	Spatial growth rate
Δt	Time step
Δx	Length interval
δ_c	Dirac delta
ε	Density ratio of gas to liquid
η	Disturbance amplitude of the jet radius

η_0	Initial disturbance amplitude of the jet radius
κ	Non-dimensional wavenumber
λ	Interface wavelength
μ	Viscosity
ξ	Perturbation of streamwise jet velocity
ξ_0	Initial perturbation of streamwise jet velocity
ρ	Density
τ	Capillary time
σ	Surface tension coefficient
ϕ	Azimuthal coordinate
ω	Growth rate
ω_r	Angular frequency
ω_i	Temporal growth rate
u	Velocity field
$\boldsymbol{g}$	Gravity
$\boldsymbol{D}$	Dimensional deformation tensor
$\boldsymbol{S}$	Dimensionless deformation tensor
n	Normal unit vector to the interface
CFL	Courant number
Fr	Froude number
Oh	Ohnesorge number
Re	Reynolds number
We	Weber number
We_c	Critical Weber number

Subscripts

b	Breakup time
g	Air
l	Liquid

Chapter 1

Introduction

A liquid jet is unstable and may break into small droplets and ligaments when emanating from a nozzle orifice into an ambient gas due to even small disturbances. These disturbances are generated by liquid/gas surface displacement on the jet surface, velocity or pressure fluctuations in the supply system and the pump used to pressurize water, as well as fluctuations in liquid properties such as temperature, viscosity, or surface tension coefficient (Ashgriz & Mashayek 1995). The study of liquid jet breakup and its instability has been a subject of interest for numerous scientific studies in the last decade (Amini et al. 2013, Erriguible et al. 2012, Jalaal & Mehravaran 2012, Wegener et al. 2014).

In order to determine the capillary jet instability, the jet characteristics, such as breakup length, detached droplet size, satellite formation, as well as its disturbance growth rate were studied (Ashgriz & Yarin 2011). Different types of disturbances have been imposed to characterize the jet instability. Oscillators can be used at the nozzles which generate disturbances by applying a periodic voltage. Velocity disturbances can be due to oscillating flow. Pressure disturbances can be introduced by applying a sound wave on the jet. Surface tension coefficient changes by temperature which can be varied by applying a periodic heating on a jet.

1.1 Importance of Liquid Jet Breakup

In a wide range of industrial applications, the issue of jet breakup and its fragmentation characteristics is significant. The physical processes such as combustion, propulsion, fluid models for atomic fusion, ink-jet printers, micro-fluidics, turbines, biomechanics, food processing and cooling systems are typical examples (Hancock & Bush 2002, Ibrahim & Akpan 1998, Percin & Khuri-Yakub 2003, Riahi 2009, Srinivasan et al. 2011).

The application of capillary jets in ink-jet printing has motivated scientists to study the breakup process of liquid jet due to recent developments in ink-jet printing techniques (Lukacs et al. 2011, Vu et al. 2013). In the ink-jet printers, the liquid jet breaks into droplets

due to inertia forces and supported by surface tension. The droplets and liquid column velocities are between 2-3 m/s (Kamphoefner 1972). The investigation of jet instability is dedicated to determine detached droplet size, ink jet breakup length in order to modify ink-jet printing quality (Heinzl & Hertz 1985).

One of the main concerns in ink-jet printing technology is to control the relatively small droplets formed when thin ligaments detach from both ends of the main droplets (Bogy 1979). These small droplets are named satellite or spherules drops. Figure 1-1 shows the breakup of a liquid jet subject to a small initial nozzle disturbance. As observed, some satellite droplets detached from the liquid column. In the ink-jet printers, it is preferred to minimize the formation of satellite droplets and have uniform breakup as shown in Figure 1-2.

Another application for capillary jet is metal formation. In order to produce uniformly sized particles and small spheres, many methods have been proposed. Minemoto et al. (2005) developed the jet-splitting technique to fabricate uniformly sized silicon particles for spherical silicon solar cells using a dropping furnace and a free-fall tower. Later, Shimasaki and Taniguchi (2011) applied electromagnetic force to a jet for increasing the production rate of silicon particles and yield of silicon particles for spherical silicon solar cells.

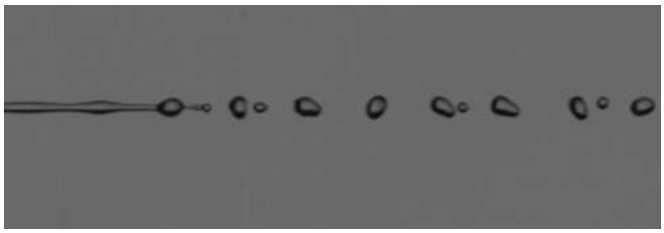

Figure 1-1: Instability of a water jet with a diameter of 0.25 mm and a velocity of 2.94 m/s with formation of satellite droplets

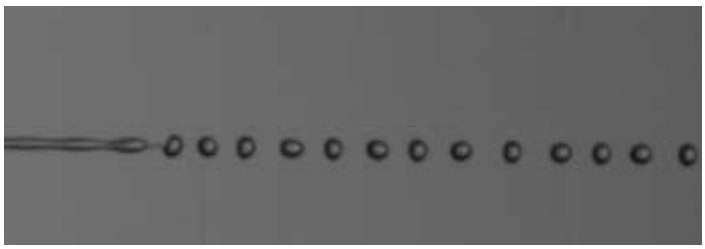

Figure 1-2: Uniform breakup of a water jet with a diameter of 0.25 mm and a velocity of 2.94 m/s

1.2 Breakup Regimes

Naturally, liquid jets are unstable and will eventually break up into smaller parts such as ligaments and droplets. Breakup modes and instabilities have been determined based on the flow parameters. Jet velocity, surface tension, viscosity, ambient pressure, and turbulence in the nozzle are some of the parameters that influence the breakup of a free jet. Analysis of these parameters can be useful in term of obtaining reliable information about the breakup length, generated droplet diameters, and dominant breakup regimes.

1.2.1 Dripping Regime

At very low velocities when momentum forces are not strong enough to overcome capillary forces, dripping occurs. In this regime, periodic and monodisperse droplets are produced with a drop size in order of nozzle diameter (Cordero et al. 2011). As inertial forces become dominant over capillary forces, the breakup of the liquid into drops is postponed and the droplets detach from the jet far downstream of the nozzle. This is the starting point for the jetting regime. With increasing jet velocities, jet breakup will exhibit four modes including Rayleigh breakup, first wind-induced, second wind-induced, and atomization (Delteil et al. 2011). As shown in Figure 1-3, four possible jet breakup regimes are distinguishable.

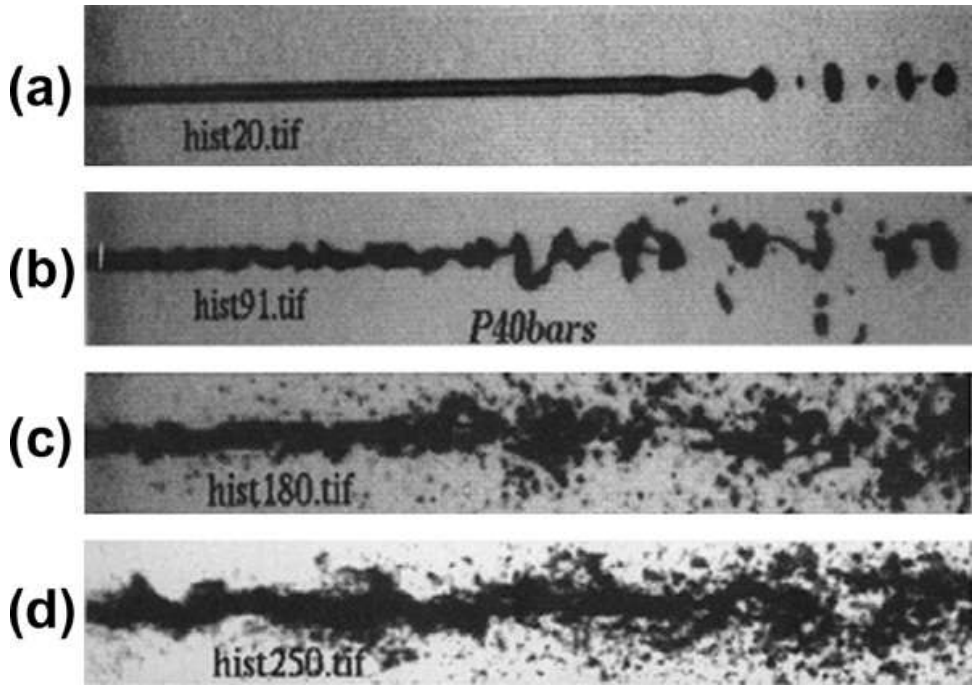

Figure 1-3: Breakup modes (modified from Delteil et al. 2011) (a) Rayleigh breakup mode, (b) first wind-induced, (c) second wind-induced, (d) atomization.

1.2.2 Rayleigh Regime

The Rayleigh regime appears by increasing the jet velocity (see Figure 1-1a). Rayleigh breakup mode still occurs for liquid jets with low velocities. Classic studies on this topic include Plateau (1873), Rayleigh (1879) and Weber (1948), which neglected the influence of the ambient air. In the Rayleigh breakup mode, the jet breakup is not under the influence of aerodynamic forces. Therefore, the capillary pinching phenomenon occurs due to surface tension forces at low jet velocities (Blaisot & Adeline 2003). Capillary instability occurs as a result of growth of interfacial disturbances by axisymmetric disturbances with wavelengths greater than the jet's circumference. The jet breaks up when the growth of the disturbance amplitude reaches the jet radius. Therefore, detachment of droplet appears with droplet diameter on the order of the jet. In this regime, a linear increase in breakup length is expected

by increasing the jet velocity. The instability of interfacial wave due to surface tension forces causes jet breakup with low jet velocities (Arai & Amagai 1999).

1.2.2.1 Theoretical Growth Rate for Capillary Instability

The surface wave on the jet surface is due to the advection of disturbance, which is imposed only at nozzle exit with a frequency, f, and initial disturbance amplitude, η_0. The disturbance is expressed by

$$\eta(x,t) = \eta_0 e^{i2\pi ft} \tag{1.1}$$

The formation of the travelling wave can also be described based on fluid particles on the jet surface. Each surface particle is displaced from its undisturbed location, a, when it is exiting the nozzle. Depending on when the particle is exiting, the initial displacement is determined by Eq. (1.1). The displacement will develop as the particle is flowing downstream.

The wave can be described both in a lab frame of reference, denoted by, $\bar{x}$, or a moving frame of reference, denoted by, x. The relation of the two frames is

$$\bar{x} = x + Ut \tag{1.2}$$

In the lab frame with its origin located at the nozzle exit, the observed surface displacement is

$$\eta(\bar{x},t) = \eta_0 e^{i(2\pi ft - k\bar{x})} e^{\beta\bar{x}} \tag{1.3}$$

where k is spatial wave number. At a downstream location, $\bar{x}$, the local amplitude is $\eta_0 e^{\beta\bar{x}}$, and β is spatial growth rate., If the fluid velocity is much larger than capillary velocity, i.e. $\frac{U}{\sqrt{\sigma/\rho_l D}} \gg 1$, the travelling speed of the wave can be considered equal to fluid velocity U. Here σ is the surface tension coefficient, ρ_l is liquid density, and D is nozzle diameter. Hence, the wavelength of the traveling wave is

$$\lambda = U/f \tag{1.4}$$

And the spatial wavenumber of the wave is

$$k = \frac{2\pi}{\lambda} = 2\pi \frac{f}{U} \tag{1.5}$$

And the temporal growth rate of disturbance (ω) is obtained by

$$\omega = U\beta \tag{1.6}$$

Substituting Equations (1.2) (1.5), and (1.6) into (1.3), the wave can be described in the moving frame as

$$\eta(x,t) = \eta_0 e^{-ikx} e^{\omega(\frac{x}{U}+t_0)} \tag{1.7}$$

Since the frame is moving at the same velocity of the jet, the equation above describes the instantaneous displacement of a fluid particle on the jet surface located at x in the moving frame. Here $\frac{x}{U} + t_0$ is the time length since the local particle was initially displaced when it was exiting from the nozzle. And the clock t_0 starts from the point when the particle located at the frame origin was initially displaced. If the surface particle at location x is being tracked, for simplicity, we let the clock start from the initial displacement of the particle, i.e. $t = \frac{x}{U} + t_0$. Hence, instantaneous displacement of the particle at location x can be expressed as,

$$\eta(x,t) = \eta_0 e^{-ikx} e^{\omega t} \tag{1.8}$$

It should be noted that the relative distance are the same in the two frames of references. Hence, the breakup length derived from the theory based on moving frame should be the same as the breakup length observed in the lab frame.

A more complete description of disturbed jets needs to include azimuthal disturbance. The description can be expressed by

$$\eta(x,\phi,t) = \eta_0 e^{i(-kx+m\phi)} e^{\omega t} \tag{1.9}$$

where x and ϕ denote the axial and azimuthal coordinate, respectively. And m is the azimuthal mode. It has been shown that liquid jets with azimuthal disturbance ($m \neq 0$) are

stable and symmetric varicose disturbances with no azimuthal mode lead to breakup (Eggers & Villermaux 2008).

Hence in the present work, no azimuthal disturbance is considered. Based on Equation (1.8), the radius of a perturbed jet is

$$R(x,t) = a + \eta_0 e^{\omega t - ikx} \tag{1.10}$$

By solving a set of mass and momentum conservation equations along with dynamic and kinematic conditions at the interface between liquid and gas, a dispersion equation was obtained. A dispersion relation between growth rate of disturbance and non-dimensional wave number has been defined by this formula which was first derived by Rayleigh (1879a) as:

$$\omega^2 = \frac{\kappa}{\tau^2}\frac{I_1(\kappa)}{I_0(\kappa)}(1-\kappa^2) \tag{1.11}$$

$\kappa = ka$ and τ (Eq. 1.11) are respectively the non-dimensional wave number and charaterstic time scale of motion.

$$\tau = \sqrt{\frac{\rho_l a^3}{\sigma}} \tag{1.12}$$

Based on the Rayleigh equation, the maximum growth rate of a disturbance is predicted to be related to a non-dimensional wave number around 0.7. For $\kappa \ll 1$, $I_1(\kappa)/I_0(\kappa) \approx \kappa/2$. Therefore, the maximum growth rate value is estimated as:

$$\omega = 0.34\sqrt{\frac{\sigma}{\rho_l a^3}} = 0.97\sqrt{\frac{\sigma}{\rho_l D^3}} \tag{1.13}$$

It is assumed that the jet breaks and droplet detaches when initial radius disturbance grows and reaches jet radius. Also, the jet breakup length, L, is estimated by considering constant jet velocity and computing the breakup time as t_b , when growth of disturbance reaches the

radius of the unperturbed jet. Therefore, the breakup length can be obtained as (Ashgriz & Yarin 2011):

$$\frac{L}{D} = 1.04\ln(\frac{a}{\eta_0})\sqrt{We} \tag{1.14}$$

where $\frac{L}{D}$ shows the ratio of breakup length to nozzle diameter and We is Weber number. The Weber number is a non-dimensional number showing the relative importance of inertia to surface tension forces. It is defined as:

$$We = \frac{\rho_l {U_0}^2 D}{\sigma} \tag{1.15}$$

For capillary jet the droplet production rate is the imposed frequency. Therefore, by increasing the frequency, the number of generated droplet is increased as long as $\kappa < 1$.

1.2.3 First Wind-induced Regime

At higher flow rates, the predictable symmetrical disturbance of the Rayleigh regime is going to disappear. The breakup mechanism starts to turn to transverse wave disintegration (Dumouchel 2008). First, Weber (1948) proposed a possible explanation for this change. He showed that the shear stress between liquid and gas at the interface of fluids due to aerodynamic forces could influence the disintegration mechanism. In other words, at high jet velocities, the dominant instability is caused by a coupling between Rayleigh instability and Kelvin-Helmholtz instability (Bremond et al. 2007). As it is shown in Figure 1-3b, the liquid jet has an asymmetrical disturbance in wavy breakup or first order wind-induced regime. In this regime, similar to Rayleigh regime, the droplets detach upstream from liquid jet (Delteil et al. 2011).

1.2.4 Second Wind-induced Regime

As a consequence of acceleration of inertia at high inlet velocities, the fluid flow begins to become turbulent and the second wind-induced mode (Figure 1-3c) appears. In this region, the fluid inertia forces can overcome aerodynamic forces or the influence of surrounding gas

resistance. Therefore, the breakup length is expended by increasing the jet velocity. On the other hand, the growth rate of the disturbance grows with assistance of liquid flow turbulence which increases the aerodynamic forces. Thus, the generation of droplets is observed at the vicinity of the nozzle.

In general, the fragmentation of droplets in this region can occur in two different zones. These two specific sub zones are named as the primary and secondary breakup (Michalke & Hermann 1982). The droplets dispersed from the coherent part of the jet in the primary breakup while the liquid jet is completely turned into small droplets in the secondary breakup (Delteil et al. 2011).

1.2.5 Atomization Regime

The atomization regime (Figure 1-3d) appears when the fragmentation of droplets starts at the nozzle exit (Sirignano & Mehring 2000). Large exchange surface between phases, especially near to the nozzle, makes this mechanism applicable for combustion benefits. Some researchers considered this breakup mode similar to the second wind-induced regime (Blaisot & Adeline 2003).

Ibrahim & Marshall (2000) did a temporal analysis for instability of a jet with relatively parabolic profile for velocity change. The authors showed the effect of surrounding air on the jet breakup. The effect was studied for jets with different values of a modified Weber number εWe, where We is the jet Weber number and ε is the density ratio of gas to liquid. According to their results, two different regimes could be dominant on jet instability based on the Weber number and the gas to liquid density ratio. When $\varepsilon We < 1$ because of capillary forces, the Rayleigh regime controls the instability. Whereas, for case $\varepsilon We > 1$, the aerodynamic forces are dominant and the atomization regime sets in. Therefore, increasing the Weber number develops the instability. Their results also demonstrated that the sizes of the generated droplets for the atomization regime are smaller than those for the Rayleigh regime. This could be because of two main reasons: 1) The jet can breakup with larger wave numbers (disturbances with shorter wavelengths); 2) The wave number corresponding to the maximum growth rate is higher.

According to various combinations of dominant forces such as capillary, aerodynamic, viscous, and inertia, the breakup regimes alter. Dumouchel (2008) used the Ohnesorge number in addition to the Weber number and the gas to liquid density ratio to categorize jet breakup regimes. The Ohnesorge number (Oh) is a dimensionless number in order to determine the relation between the viscous forces and surface tension and inertia forces. It is defined as:

$$Oh = \frac{\mu_l}{\sqrt{\rho_l \sigma D}} \tag{1.16}$$

where μ_l denotes liquid viscosity. As shown in Table 1-1, the disintegration regimes are classified corresponding to these non-dimensional numbers.

Table 1-1 Disintegration breakup regimes corresponding to Weber number criteria (From Dumouchel 2008)

Disintegration regime	Weber number criteria
Dripping	$We < 4$
Rayleigh	$We > 4, \varepsilon We < 0.6 + 2.5Oh^{0.9}$
First wind-induced	$0.6 + 2.5Oh^{0.9} < \varepsilon We < 6.5$
Second wind-induced	$6.5 < \varepsilon We < 20.15$
Atomization (Spray)	$\varepsilon We > 20.15$

1.2.6 Effect of Dominant Regime on Breakup Length

The velocity difference between the liquid and the surrounding gas is one of the characters that the mode of jet disintegration is completely relevant to. First, Grant and Middleman (1966) claimed that the jet instability could be described by the response of the coherent part of the jet or the influence of the jet velocity on breakup length. Their experimental results

indicated relations between the jet velocity (*U*) and the breakup length (*L*). The distance between the nozzle exit and the far end of the continuous jet is referred to as breakup length. As shown in Figure 1-4, four different zones of fragmentation for breakup length can be distinguished.

The part *ABC* when the velocity is lower than V_0 represents the dripping regime and does not generate a jet. Dripping liquid rises from the nozzle exit at very low flow rates. The desirable operating velocity is usually higher than V_0. So, extrapolating the line of the DC section through the initial dripping part could be acceptable way to ignore the dripping regime (Grant & Middleman 1966). The linear section of the instability curve (*ACD*) is related to the case with low jet velocity and ambient gas. The jet breakup is not under the influence of aerodynamic forces. Therefore, the capillary pinching phenomenon occurs due to the impact of surface tension forces (Blaisot & Adeline 2003). This breakup mode is named Rayleigh. Figure 1-5 shows the experimental results for the breakup length for the Rayleigh mode. As observed, the breakup length is increased by increasing the initial jet velocity at the nozzle exit.

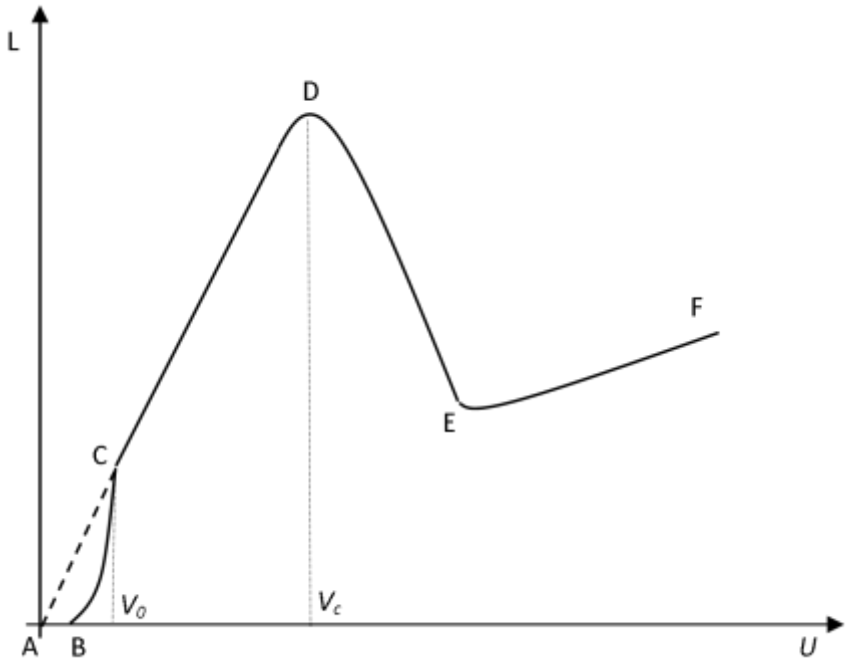

Figure 1-4: Effect of dominant regime on breakup length and instability. Dependance of jet breakup length on the jet velocity.

The influence of nozzle geometry on jet breakup and on the size of its spray droplets were demonstrated in Karasawa et al. (Karasawa et al. 1992). The transition between the Rayleigh and the wavy breakup modes occurs at the critical point (point *D* in Figure 1-4). The critical point changes due to the velocity profile development which is effected by the nozzle length (Leroux et al. 1996). In part DE, as it was shown in the instability carve figure, although the jet velocity is increased, the breakup length decreases due to the aerodynamic effects. In this region, the first wind-induced mode sets in. Figure 1-6 shows the reduction of breakup length for the first wind-induced mode with a higher jet velocity (after critical point) compared to the Rayleigh breakup mode with a lower jet velocity (before critical point). At higher velocities (*EF*), the mechanism of breakup changes progressively to the second wind-induced mode and atomization regimes (Lin & Lian 1990).

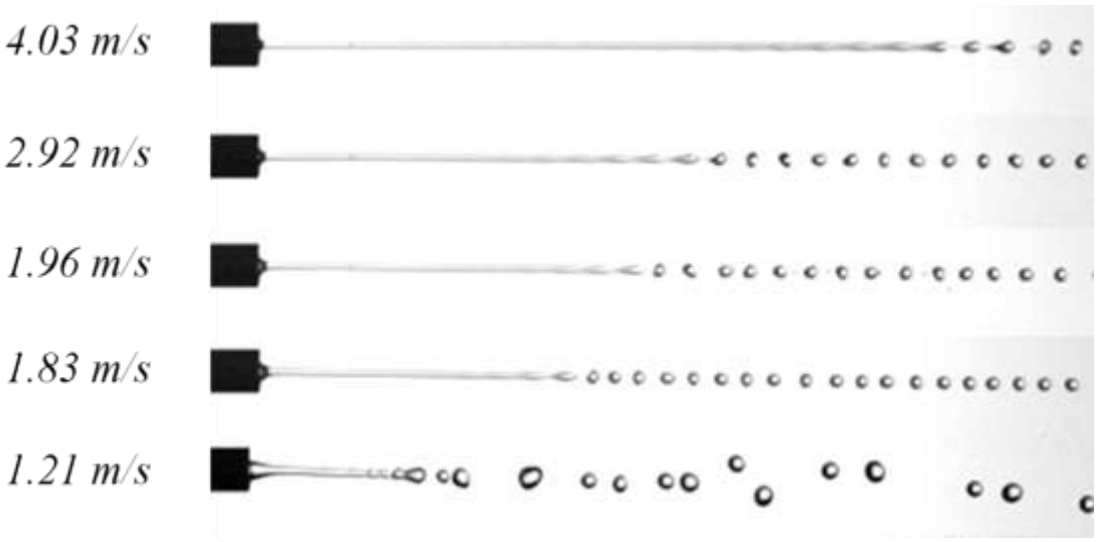

Figure 1-5 Increasing the jet breakup length by jet velocity in the Rayleigh regime.

Figure 1-6 Jet breakup length for Rayleigh mode (Case A) with mean jet velocity 4.03 m/s in comparison with first wind-induced (case B) with mean jet velocity 9.98 m/s.

1.3 Capillary Jet Breakup

First, Plateau (1873) studied the surface energy of a uniform liquid cylinder for a given jet volume. He pointed out that the cylindrical liquid shape has a tendency to break into small portions with length equal to its circumference. Rayleigh (1879a, 1879b) considered an inviscid liquid jet and argued that a liquid jet disintegrates as a consequence of hydrodynamic instability. His dispersion relation was obtained based on solving the kinetic and potential energy equations in this classical study. This equation defines a relation between the

wavenumber of the disturbance and the growth rate of the amplification. He demonstrated that the jet is unstable with respect to the disturbance with a wavelength larger than its circumference. Based on his dispersion relation equation, among all unstable disturbances, the maximum growth rate of the disturbance is related to disturbance with a non-dimensional wavenumber around 0.7. Moreover, the calculated droplet diameter by applying the mass conservation equation at the breakup is 1.89 times larger than the unperturbed jet diameter.

Later, Rayleigh tried to expand his theory by adding the effect of viscosity but no applicable results was proposed from his excessively complicated analysis. The influence of liquid viscosity on Rayleigh breakup instability was studied by Weber (1948). Base on his finding, the cut-off wave number was not affected by the liquid viscosity. However, it dampens the instability and shifts the maximum growth rate toward smaller wave numbers. Weber and Rayleigh estimated the drop size for a wavenumber around 0.7 . In addition, Weber also illustrated that the droplet size increases due to a lower growth rate, considering the effect of viscosity.

Taylor (1962) considered the effect of surrounding gas density and revealed its fundamental influence on the jet breakup regime. The effect of the surrounding gas is more important when the capillary forces are sufficiently smaller than the gas inertia forces at the liquid-gas interface. Therefore, the surrounding gas effect appears on the atomization regime and leads to droplet formation with a diameter much less than the jet diameter.

The comprehensive knowledge and theories about breakup process are explained in a few review papers such as Sirignano (1993), Chigier and Reitz (1996), and Lin and Reitz (1998).

A lot of experimental work has been done to investigate the breakup of liquid jets in the Rayleigh regime. Malot and Blaisot (2000) used an image analysis technique to measure the distribution of droplet size for low velocity cylindrical liquid jets. In order to analyze the measurements, spherical and non-spherical droplets were categorized based on shape parameters. The backlight image was analyzed to determine the droplet size distribution for each individual truly spherical droplet. Kalaaji et al. (2003) studied breakup of a liquid jet due to sinusoidal velocity disturbances by a laser photometry method. The breakup length was measured for a wide range of jet velocities with various fluid viscosities in the Rayleigh and the first-wind induced regimes. Cheong and Howes (2004) investigated the influence of

gravity on capillary jet instability. González and García (2009) experimentally demonstrated growth rate of disturbance on capillary jet using Electro Hydro Dynamic (EHD) sinusoidal stimulation. Rohani et al. (2010) applied a manipulated disturbance by a piezoelectric actuator to provide a manipulated disturbance in order to control the droplet generation rate and breakup length. By changing the velocity frequency, the desired droplet size and breakup length were generated for sinusoidal and composite disturbances. Their experimental result demonstrates that breakup length and droplet size can be adjusted by using composite velocity disturbances and controlling the frequencies and amplitudes. Later, Shimasaki and Taniguchi (2011) used electromagnetic forces to characterize droplet production rate of the capillary jet of liquid metal. In their study, a capillary jet of liquid metal is used as an applicable method in order to produce uniform droplets of melted metal.

In addition to experimental approaches, the numerical simulation is a helpful tool to understand the main physical process of the flow and jet breakup. Due to the improvement of numerical techniques, the application of direct numerical simulation methods such as Volume of Fluid (VOF), level set and front-tracking methods describing the behavior of multiphase flows in jet breakup have become popular. The VOF method is one of the most widely used techniques dealing with the interface of two phase flows. This method is based on an advection scheme which uses fraction function to determine volumetric fraction of reference phase in each grid cell (Cervone et al. 2010).

Richards et al. (1994) conducted one of the first numerical studies of liquid jet instability using the 2D dynamic breakup by means of VOF methods. The axisymmetric, dynamic breakup for Newtonian liquid jet injected into another immiscible Newtonian liquid was studied at different Reynolds numbers. Sussman and Puckett (2000) investigated the jet breakup in the Rayleigh regime using a coupled level set and VOF method. Their study was focused on a computational algorithm to model a 3D axisymmetric problem for incompressible two-phase flows. Coupled level set/volume of fluid (CLSVOF) method is used in order to improve computational accuracy of the free-surface in two-phase flow problems and to model micro scale jetting devices. Pan & Suga (2006) applied level-set methods to study the breakup process of a laminar liquid jet. The breakup phenomenon is analyzed for various ranges of Weber and Ohnesorge numbers to modify a conventional

classification diagram for breakup mechanism. Ménard et al. (2007) investigated the jet breakup in the Rayleigh regime using a coupled level-set-ghost-fluid approach. In their numerical simulation for the primary breakup of a liquid jet, the VOF method is used for mass conservation, sharp discontinuities for viscosity, density, and pressure are captured accurately by the ghost fluid method (GFM), and also the level set method is applied in order to track the interface between liquid and gas. Zhang et al. (Zhang et al. 2010) studied capillary jet breakup by a Arbitrary Lagrangian-Eulerian (ALE) method coupled with a direct boundary tracking technique. Delteil et al. (2011) analyzed the Rayleigh breakup of round liquid jets with VOF methods.

Although theoretical studies, numerical simulations, and experimental approaches are devoted to define the details of the jet breakup process, some unclear details such as velocity profile still exist. Pan and Suga (2006) concluded in their article that further studies on the influence of the velocity profile are needed.

1.4 Objectives

The most commonly observed breakup of capillary jets is water jets breaking up into droplets in air. Understanding the breakup of capillary jets is important to many engineering applications based on liquid jets, for which the fluid is water or has properties similar to water.

Although there have been many previous studies on the breakup of capillary jets, there are still questions regarding water jets.

1) The Rayleigh theory neglects fluid viscosity and ambient air. When applied to water jets, how does the theoretical prediction compare with actual breakup of the jets?
2) What are the fluid dynamics involved in jet breakup, which include the dynamics of the jet flow and ambient air?

The major objective of the present work is to address these two questions. In the present work, the breakup of capillary water jets in quiescent ambient air is studied numerically and experimentally in comparison with the Rayleigh theory. Numerical simulations based on

VOF provide detailed fluid dynamics. Experimental tests using high speed photography provide experimental validation. Major tasks carried out in this works include:

- Performing the numerical simulation based on adaptive grids which allows us to follow the instability and breakup process and track the interface to smaller scales. Numerical results are obtained by applying high resolution for adaptive mesh refinement in the interfacial surface.
- Computing the growth rate of disturbance using liquid interface tracking.
- Conducting experimental analysis to validate numerical results and compare with Rayleigh theory.
- Extracting the jet velocity profile and pressure distribution especially in the necking region.
- Developing Lagrangian particle approach to illustrate the trajectory of liquid elements (path lines) and to evaluate the flow motion in radial direction.

1.5 Thesis Outline

The organization of this thesis is based on four chapters. In the chapter 1, which primarily has been discussed, the different mechanisms of liquid-jet breakup and its relevant parameters were described according to previous studies in this area. Methodology follows in the second chapter with demonstrating of the details of the numerical method, experimental setup, and the procedures that we used. The third chapter shows results with comprehensive analysis for the deformation and mechanism behind the breakup of free and forced jets. Conclusion and a view to the future work are presented in chapter 4. The appendix shows the data used to check mesh independency and uncertainty of results.

Chapter 2

Materials and Methods

As described in the first chapter, the breakup characteristics for free and oscillated jets are studied in this thesis. In this section, first, the governing equations and their boundary conditions are presented. Also experimental and numerical methodologies used in order to analyze the Rayleigh regime are described.

2.1 Geometries and Governing Equations

For these cases, a liquid jet is produced from a nozzle with an unperturbed jet radius, a, at a mean jet velocity U_0 and out into a quiescent gas. The physical problem configuration is illustrated in Figure 2-1.

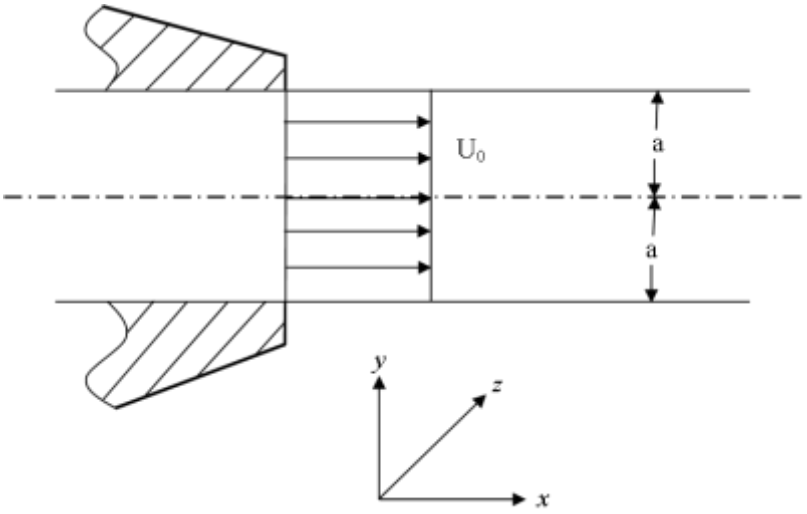

Figure 2-1: Physical problem configration in the cartesian coordinate system.

In the present numerical model, the jet has a uniform velocity profile at the nozzle exit. However, in reality, the velocity profile of a well-developed internal flow in a circular tube is

parabolic. When the liquid released from the nozzle, the liquid velocity profile will relax from parabolic toward uniform, depending on the interaction with the ambient air. For a free jet, a finite length is required for gradual relaxation from parabolic toward uniform velocity profile, and this length is referred to as intact length (Eroglu et al. 1991). Ibrahim and Marshall (2000) investigated the effect of velocity profile on the instability of liquid jet. Their analysis indicates that uniform velocity profile can be assumed in the study of the liquid jet instability because the intact length is much smaller than the jet breakup length.

For this case, a box with the size of $(8D \times 8D \times 24D)$ is considered and an initially liquid column with velocity equal to unperturbed jet velocity at the nozzle is placed in the quiescent gas at the box. The simulation initiates with uniform mesh refinement (for whole computational domain) equal to the finest mesh size used in the next time steps for mesh adaptation. The schematic figure for initial condition of simulations and the boundary condition of the computational domain is illustrated in Figure 2-2. All of the simulations in this study are performed in three dimensions.

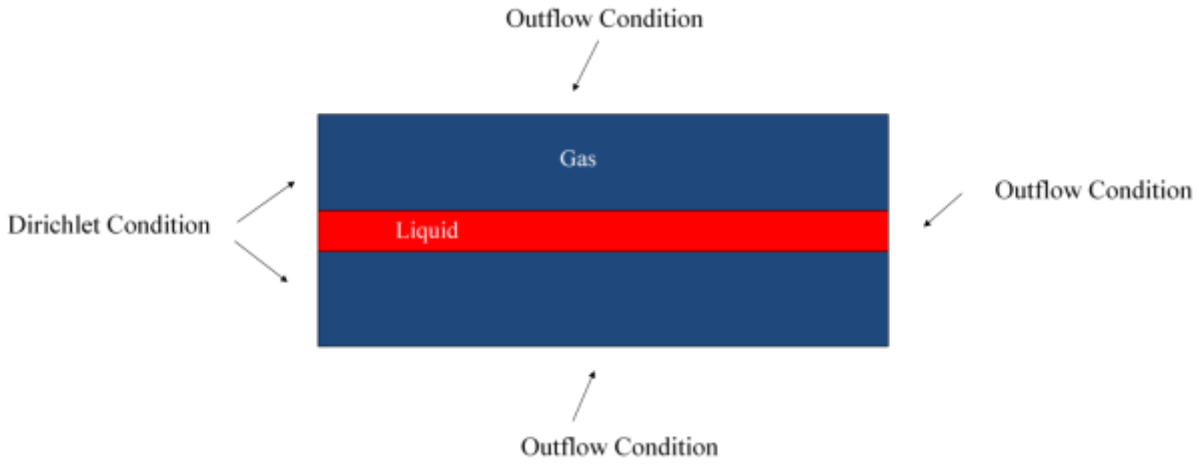

Figure 2-2: Schematic for the boundary and initial conditions for simulation of liquid jet

2.1.1 Governing Equations

The two phases, jet and ambient air, are treated as incompressible fluids. The set of governing equations for the liquid and gas phases are iso-thermal Navier-Stokes equations (Eq. 2.1),

$$\rho_i \left(\frac{\partial \mathbf{u}_i}{\partial t} + \mathbf{u}_i \cdot \nabla \boldsymbol{u}_i \right) = -\nabla p_i + \rho_i \boldsymbol{g} + \mu_i \nabla^2 \mathbf{u}_i \tag{2.1}$$

and the continuity equation,

$$\nabla \cdot \mathbf{u}_i = 0 \tag{2.2}$$

where the subscript $i = l$ represents liquid, and $i = g$ represents air. $\mathbf{u}$ shows the three components (u_x, u_y, u_z) of the velocity field. x and t denote the axial distance and time, respectively. p is the fluid pressure. $\boldsymbol{g}$ is the acceleration due to gravity. ρ and μ denote the density and viscosity of the fluids, respectively.

2.1.2 Boundary Conditions

In the cases with interfaces, two different types of boundary conditions represent the interface conditions: 1) the stress balance, and 2) kinematic boundary condition. One of the major factors in the evolution of the liquid surface shape at the multiphase flow interface is the stress balance. This stress is implemented by both the viscous and the surface tension forces (Eq. 2.3).

$$\left(p_l - p_g + \sigma H\right)\mathbf{n} = \left(\boldsymbol{\tau}_l - \boldsymbol{\tau}_g\right) \cdot \mathbf{n} \tag{2.3}$$

where $\mathbf{n}$ and $\boldsymbol{\tau}$ are normal unit vector to the interface and stress tensor respectively. With this assumption that the surface has an infinitesimal thickness, the mean interface curvature, H, is written as,

$$H = \nabla \cdot \mathbf{n} = \frac{1}{R_1} + \frac{1}{R_2} \tag{2.4}$$

where R_1 and R_2 are the principal radii of curvature of the interface in the *xy*- and *yz*-plane respectively.

Based on the kinematic boundary condition, the velocity component normal to the interface is continuous across the interface. This boundary condition indicates that the fluid does not cross the free-surface (Eq. 2.5).

$$\mathbf{u}_l \cdot \mathbf{n} = \mathbf{u}_g \cdot \mathbf{n} \tag{2.5}$$

The boundary condition which is considered here is for breakup of axisymmetric jets.

2.2 Numerical Method

In order to justify and trace the interface of the two-phase flow, a volume fraction function *c* is introduced. A volume fraction function *c* is defined as a volume fraction of liquid as,

$$c(x,t) = \begin{cases} 0 & gas \\ 0 < c < 1 & liquid/gas\ \ interface \\ 1 & liquid \end{cases}. \tag{2.6}$$

The volume fraction function determines the volume fraction of liquid in each cell of the computational mesh which is located at interface of liquid and gas, and the density and viscosity can be calculated as,

$$\rho(c) = c\rho_l + (1-c)\rho_g, \tag{2.7}$$

$$\mu(c) = c\mu_l + (1-c)\mu_g. \tag{2.8}$$

According to the liquid surface advection by the velocity field, it is necessary to observe the spatial and temporal evolution. Consequently, based on the volume-of-fluid (VOF) method, the continuity equation for density can be replaced with volume fraction function:

$$\frac{\partial c}{\partial t} + \nabla \cdot (c\mathbf{u}) = 0. \tag{2.9}$$

2.2.1 Non-Dimensional Equations and Parameters

The quantities for nondimensionalizing the governing momentum and continuity equations are defined by using the nozzle radius and the mean jet velocity as,

$$\mathbf{u}' = \frac{\mathbf{u}}{U_0} \quad , \quad p' = \frac{p_i}{\rho_l {U_0}^2} \quad , \quad x' = \frac{x}{a} \quad , \quad t' = \frac{U_0}{a} t \tag{2.10}$$

when prime refers to a dimensionless quantity. To clarify the physical meaning of the effective variables, it is helpful to use appropriate dimensionless parameters. In the case of a jet breakup, the Reynolds number can be defined:

$$Re = \frac{\rho_l U_0 D}{\mu_l}; \tag{2.11}$$

We and Re are the Weber and Reynolds numbers of the liquid, respectively. The Froude number,

$$Fr = \frac{{U_0}^2}{gD} \tag{2.12}$$

represents the ratio of inertia to gravitational forces. It was found from our simulations that the effect of gravity is negligible in high Froude numbers. The gravitational effects can be neglected once Fr>5000 at high injection velocities (Sander & Weigand 2008). The density and viscosity ratios are two other important parameters:

$$\varepsilon = \frac{\rho_g}{\rho_l} \tag{2.13}$$

$$M = \frac{\mu_g}{\mu_l} \tag{2.14}$$

2.2.2 Non-dimensional Governing Equations and Boundary Condition

In the VOF method, the volume fraction of a fluid in each grid cell of the computational mesh is determined. The set of non-dimensional equations for the continuity, momentum, and volume fraction can be written as:

$$\nabla \cdot \mathbf{u}' = 0. \tag{2.15}$$

$$\left(\frac{\partial \mathbf{u}'}{\partial t'} + \mathbf{u}' \cdot \nabla \mathbf{u}'\right) = -\frac{\nabla p'}{\varepsilon} + \frac{1}{2Fr} + \frac{2\nabla^2 M\mathbf{u}'}{\varepsilon Re} \tag{2.16}$$

$$\frac{\partial c}{\partial t'} + \nabla \cdot (c\mathbf{u}') = 0 \tag{2.17}$$

The normal stress condition assumes the dimensionless form:

$$(p'_l - \varepsilon p'_g + \frac{2}{We}\nabla \cdot \mathbf{n})\mathbf{n} = \frac{4}{Re}(\boldsymbol{S_l} - M\boldsymbol{S}_g) \cdot \mathbf{n} \tag{2.18}$$

where $\boldsymbol{S} = S_{ij} = \frac{1}{2}(\partial_i u_j + \partial_j u_i)$ is the dimensionless deformation tensor.

2.2.3 Flow Solver (Gerris)

The numerical model is built using an open source code, Gerris. Gerris is an open source code for the solving 2 or 3 dimension Navier-Stokes equations. The source code is available free of charge under the Free Software GPL license. Gerris is developed in C and supported by NIWA (National Institute of Water and Atmospheric research) in New Zealand and Institut Jean le Rond d'Alembert in France. The code brings in facilities to model plenty of industrial fluid mechanic and aerodynamic cases. This tool for computational fluid dynamics named after the insect that can move quickly over the surface of the water. It is because of its high efficiency and accuracy to simulate multiphase flows involving surface tension (Popinet 2009)

Its finite-volume discretization techniques allow solving the time-dependent incompressible variable-density Euler and momentum equations. The main feature of the code is the octree adaptive mesh refinement (i.e. the resolution is adapted dynamically to the features of the flow) with entirely automatic mesh generation in complex geometries (Popinet 2003). For this reason, second-order discretization in space and time has been employed. For the direct numerical simulation of multiphase flows, Gerris implements modern interface-tracking methods such as high-accuracy piecewise-linear volume-of-fluid (VOF) methods (Agbaglah et al. 2011).

On the other hand, Gerris was written with parallel computation structure to decompose a computational domain. Domain decomposition is achieved by splitting the main computational mesh into subdomains. In fact, parallelism beside adaptivity is another feature of this code. Later, VOF and Lagrangian particle-tracking model are combined in order to describe the effect of small droplet in the interface and motion of fluid particles inside the flow (Tomar et al. 2010).

2.2.4 Temporal Discretization

A second-order accurate time discretized equation for solving multiphase incompressible flow is presented, using a staggered in time discretization of volume-fraction/density and pressure fields (Jalaal 2012):

$$\rho_{n+\frac{1}{2}}\left(\frac{\mathbf{u}_{n+1}-\mathbf{u}_n}{\Delta t}+\mathbf{u}_{n+\frac{1}{2}}\cdot\nabla\mathbf{u}_{n+\frac{1}{2}}\right) = -\nabla p_{n+\frac{1}{2}}+\nabla\cdot\left\{\mu_{n+\frac{1}{2}}(\mathbf{D}_n+\mathbf{D}_{n+1})\right\}+(\sigma\kappa\delta_s)_{n+\frac{1}{2}}, \tag{2.19}$$

$$\frac{c_{n+\frac{1}{2}}-c_{n-\frac{1}{2}}}{\Delta t}+\nabla\cdot(c_n\mathbf{u}_n)=0, \tag{2.20}$$

$$\nabla\cdot\mathbf{u}_n=0, \tag{2.21}$$

where $\delta_s$is Dirac delta to ensure that surface tension forces only exist on the interface of liquid and air. $\mathbf{D}=D_{ij}=(\partial_i u_j+\partial_j u_i)$ denotes the deformation tensor. These are

dimensional equations. To make them non-dimensional, the Eqs. (2-15) to (2-17) should be used for discretization. By means of the classical time-splitting projection method (Chorin 1969) the discretized set of equation can be modified as,

$$\rho_{n+\frac{1}{2}}\left(\frac{\mathbf{u}_*-\mathbf{u}_n}{\Delta t}+\mathbf{u}_{n+\frac{1}{2}}\cdot\nabla\mathbf{u}_{n+\frac{1}{2}}\right)=\nabla\cdot\left\{\mu_{n+\frac{1}{2}}(\mathbf{D}_n+\mathbf{D}_*)\right\}+(\sigma\kappa\delta_s)_{n+\frac{1}{2}}, \tag{2.22}$$

$$\frac{c_{n+\frac{1}{2}}-c_{n-\frac{1}{2}}}{\Delta t}+\nabla\cdot(c_n\mathbf{u}_n)=0, \tag{2.23}$$

$$\mathbf{u}_{n+1}=\mathbf{u}_*-\frac{\Delta t}{\rho_{n+\frac{1}{2}}}\nabla p_{n+\frac{1}{2}}, \tag{2.24}$$

$$\nabla\cdot\mathbf{u}_{n+1}=0. \tag{2.25}$$

The Poisson equation governing the pressure field can be obtained using Eqs. (2.24) and (2.25) as follows:

$$\nabla\cdot\left(\frac{\Delta t}{\rho_{n+\frac{1}{2}}}\nabla p_{n+\frac{1}{2}}\right)=\nabla\cdot\mathbf{u}_* \tag{2.26}$$

The Poisson equation is efficiently estimated the pressure using equation (2.26). The velocity advection term in the discretized Navier-Stokes equation (2.22) is estimated using the robust second-order upwind scheme of Bell-Colella-Glaz (Bell et al. 1989). This scheme is stable as long as CFL numbers are smaller than one. CFL (Courant–Friedrichs–Lewy) is a dimensionless number and its value is necessary for stability of numerical results while solving discretized equations. The CFL number expresses the relationship between time step and length interval. For one-dimensional case, the CFL number is defined as

$$CFL=\frac{|\mathbf{u}|\Delta t}{\Delta x} \tag{2.27}$$

where Δt is the time step and Δx is the length interval. The viscous terms are defined by Crank–Nicholson discretization which is unconditionally stable and has second order of accuracy in time (Tomar et al. 2010). The volume fraction in Eq. (2.20) is computed using a piecewise-linear geometrical Volume of Fluid (VOF) scheme. The geometrical VOF scheme

is established based on two main steps, interface reconstruction and interface advection (Popinet 2009). The velocity and pressure fields are determined by collecting data for pressure, velocity and tracer in each computational cell. An approximate projection method is applied to decouple these fields for the spatial discretization of the pressure correction equation and the associated divergence of the auxiliary velocity (Almgren et al. 2000). The comprehensive details about auxiliary velocity field and pressure correction can be found in the recent work done by Tomar et al. (2010).

2.2.5 Spatial Discretization

Application of quadtrees (2D) and octrees (3D) for adaptive spatial discretization might be the major characteristic of the Gerris code. This type of discretization for quadtrees is shown in Figure 2-3. The main root cell which is illustrated by dotted lines is divided into four children cells for 2D and eight children cells in 3D for each level of adaptation. Different levels of adaptive spatial mesh discretization are shown in this figure. In this discretization, each neighboring cell cannot directly refine more than one level.

Different criteria can be used to do the grid refinement. The velocity gradient is one of the significant parameters that can be considered to adapt the resolution in regions where more accuracy is expected. For case of two-phase capillary jet simulation, the interface between liquid and gas can be considered as other refinement criteria because the influence of the disturbance of the carrier phase (liquid) on the jet interface and an accurate prediction of its growth rate are essential to the breakup process. The gradient of the streamwise and transverse components of the velocity is other significant parameter that should be considered as a criterion to adapt meshes for higher accuracy.

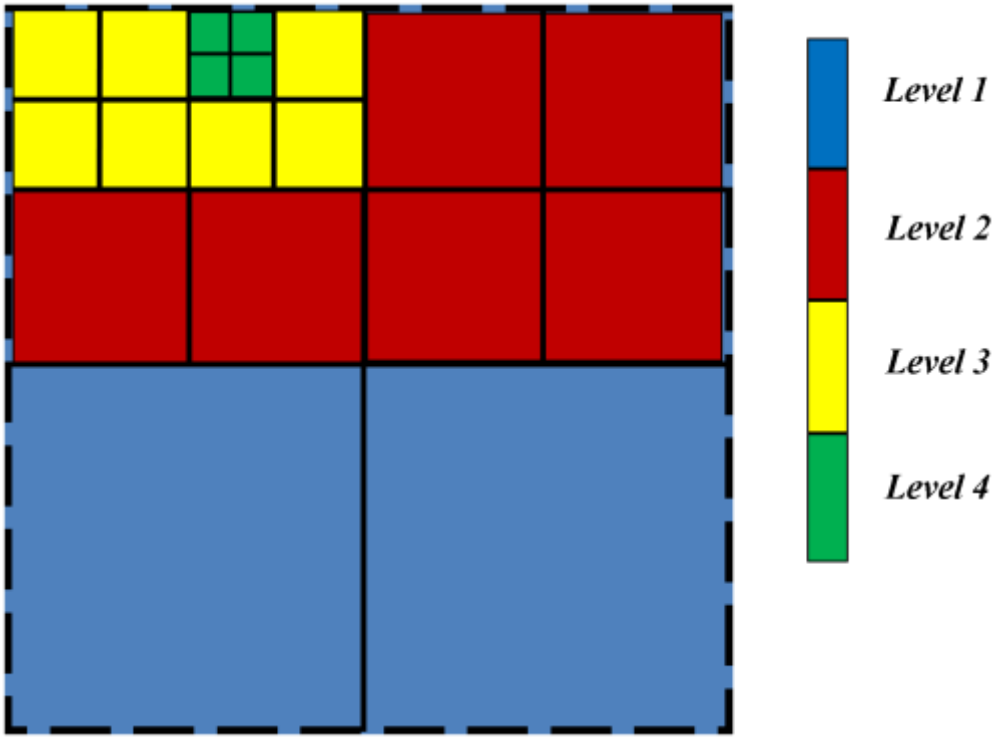

Figure 2-3: Quadtree discretisation of an adaptive mesh

For the current simulations, an adaptive 3D spatial discretization is used. Simulations are performed with varied mesh resolutions, refinements 6, 7, and 8. In order to check the mesh dependency, breakup length to the nozzle diameter ratio is compared for three different mesh refinements. The mesh dependency is tested for these refinements using t-test (see Appendix). In addition, growth rate of disturbance and interface position in the necking region are compared. Analysis of data shows quite similar results for refinement 7 and 8. Therefore, although, refinement 7 is good enough to obtain accurate results, refinement 8 is selected for the numerical study in current study.

As shown in Figure 2-2, the simulation starts with liquid column which is initially placed in the quiescent gas. The steady state condition starts after the initial liquid column breaks into droplets which go out of the computational domain. The time taken to reach steady state is $t' = 48$. The total simulating time is $t' = 320$ which is much longer than steady state time.

Saving of computational time as well as making the simulations more feasible are two other advantages of octree mesh using adaptive mesh refinement (Fuster et al. 2009). An example of mesh refinement for the centre-plane of a 3D simulation of a liquid jet breakup is shown in Figure 2-4. The finest mesh grids appear at the interface where the higher accuracy for results is expected.

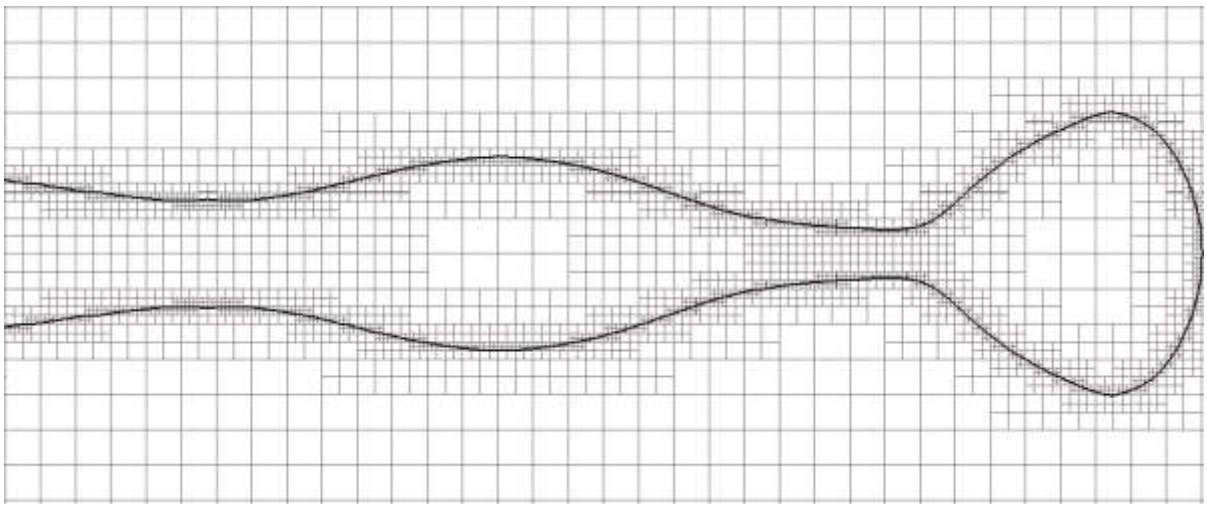

Figure 2-4: Adaptive mesh generated for a case of jet instability ($We = 29.6$ and $Re = 840$). Cross-section of the capillary jet in $z = 0$ plane

Figure 2-5 shows a series of images to present how adaptive meshing works. As observed, the mesh refinement is adapted based on the proximity to the liquid/gas interface. At different times, when the interface moves forward, the adaptive meshing changes as well. The result shows a fine mesh for not only jet interface but also satellite and detached droplet interfaces. Also, in this case, a high grid resolution for the orifice outlet is considered. Changes in velocity profile at the orifice outlet and growth of initial disturbance at this zone are two main reasons for required high accuracy at this region.

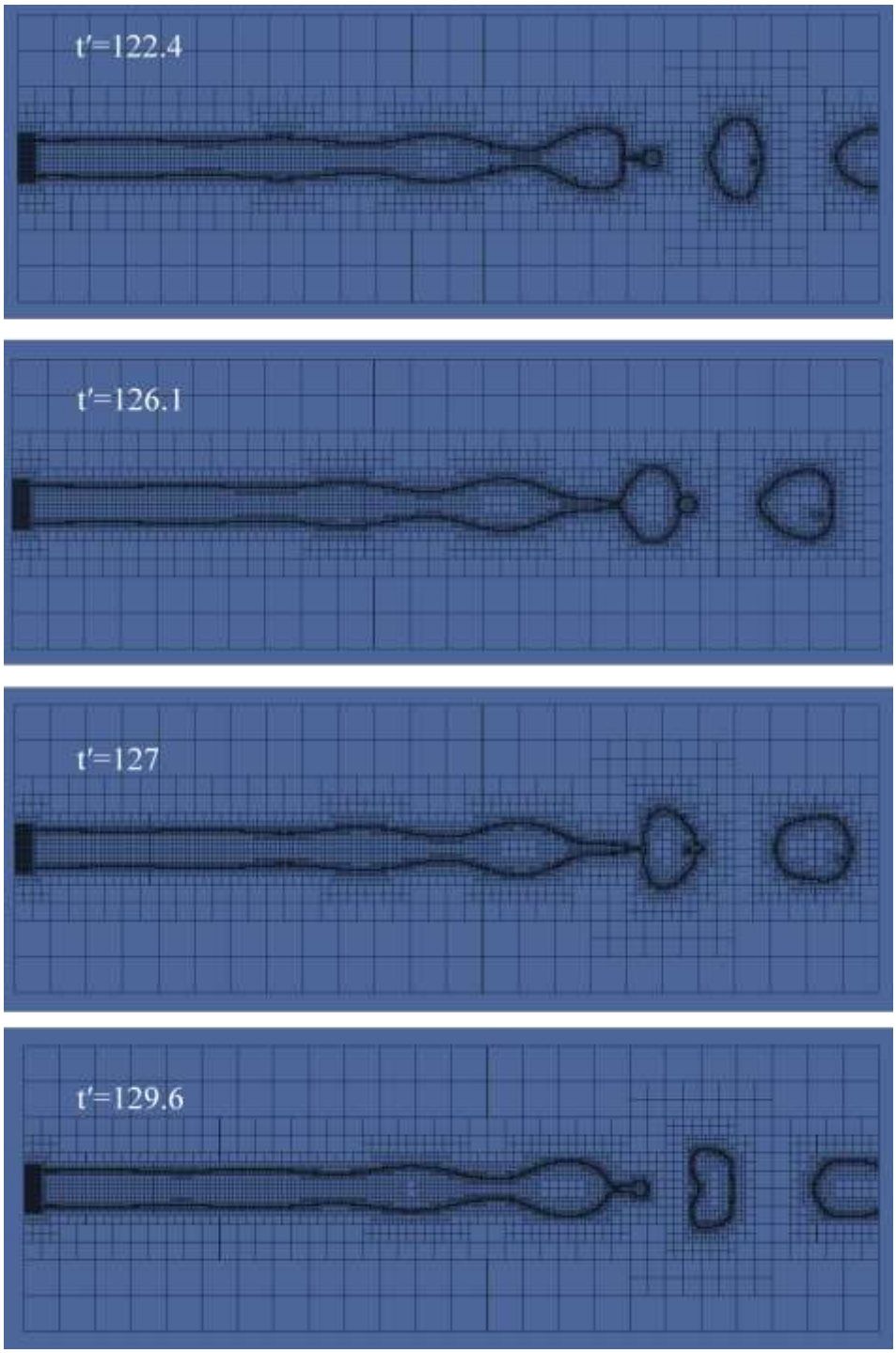

Figure 2-5: Series of images for adaptive mesh generation based on liquid/gas interface

2.3 Experimental Analysis

In this section, the experimental study has been performed to investigate the effect of jet velocity and vibrational parameters on breakup characteristics. For this purpose, the behavior of both undisturbed and disturbed jets was studied. In the undisturbed jet instability case, the breakup length was measured. In this case, the disturbance is growing based on experimental setup vibration or velocity fluctuation subject to pump oscillation. In the case of disturbed jet breakup, the instability of liquid jets which is subject to anti-symmetrical nozzle displacement was investigated. The small vibrational amplitude was imposed with a wide range of frequencies to find the growth rate of linear jet stability theory. The figures of the breakup length versus the excitation frequency are shown in chapter 3. Also, the experimental results are compared with the theoretical dispersion relation equation which is derived by Rayleigh theory as well as numerical dispersion curves which are obtained by Gerris. The breakup length and maximum growth rate have been measured in a wide range of Weber numbers.

2.3.1 Experimental Setup

Figure 2-6 illustrates schematic diagrams for experimental setup. A function generator (Tektronix AFG3021B) digitally produces a low voltage signal with specific amplitude and frequency. In particular, sinusoidal voltage signals are applied in the experiment. The low voltage signal is amplified by a high voltage amplifier to feed the nozzle oscillator. To validate the accuracy of high voltage signal and efficiency of amplifier, a digital oscilloscope (Tektronix TDS2012C) is used. By changing the voltage at the function generator, the amount of energy delivered to the oscillator was adjusted. It is the most practical way to control the initial disturbance amplitude.

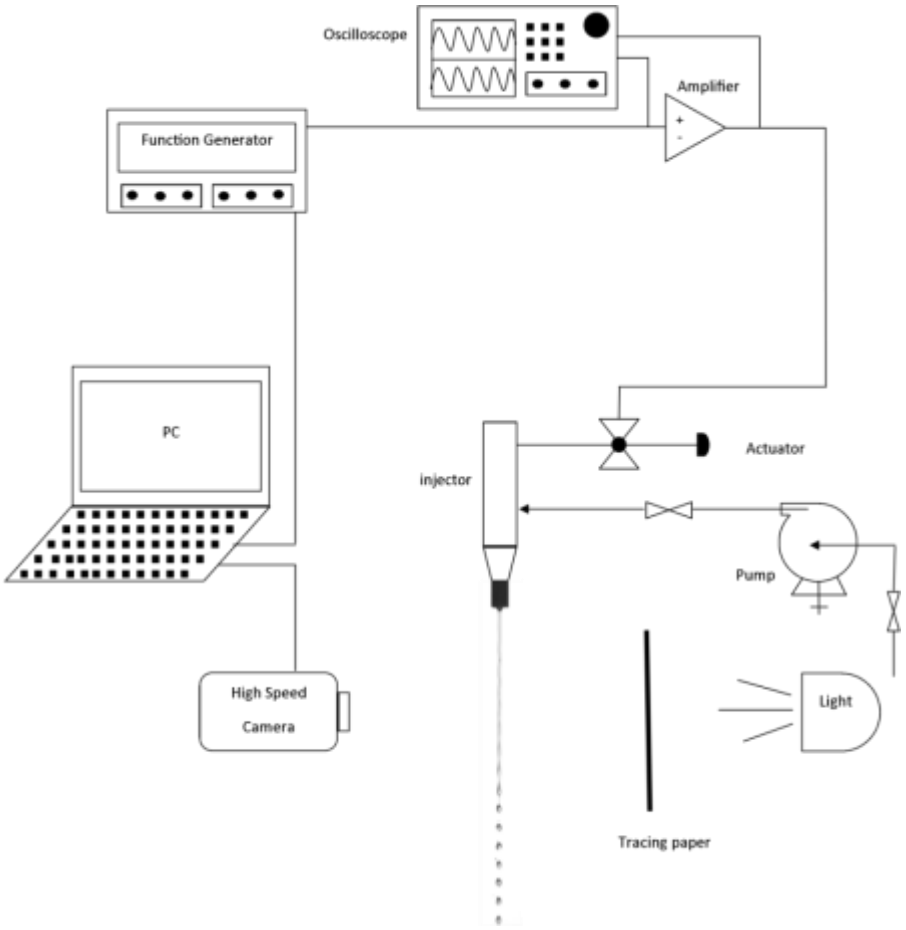

Figure 2-6: The schematic of experimental setup

As shown in Figure 2-7, the nozzle injector is directly connected to the mechanical wave driver oscillator (Pasco Scientific SF-9324). The liquid surface disturbance is generated with respect to initial disturbance amplitude and frequency of oscillator. The required visualization for this study is obtained by means of a high speed camera. For this experiment, the imposed frequency and jet velocity can be used in order to determine the required frame rate for the high speed camera. For instance, a higher frame rate is required at higher frequencies to capture the nozzle movement. In this case, 20,000 frames per second are used

to do the high speed photography. In order to adjust the light intensity, a diffused backlight system was provided.

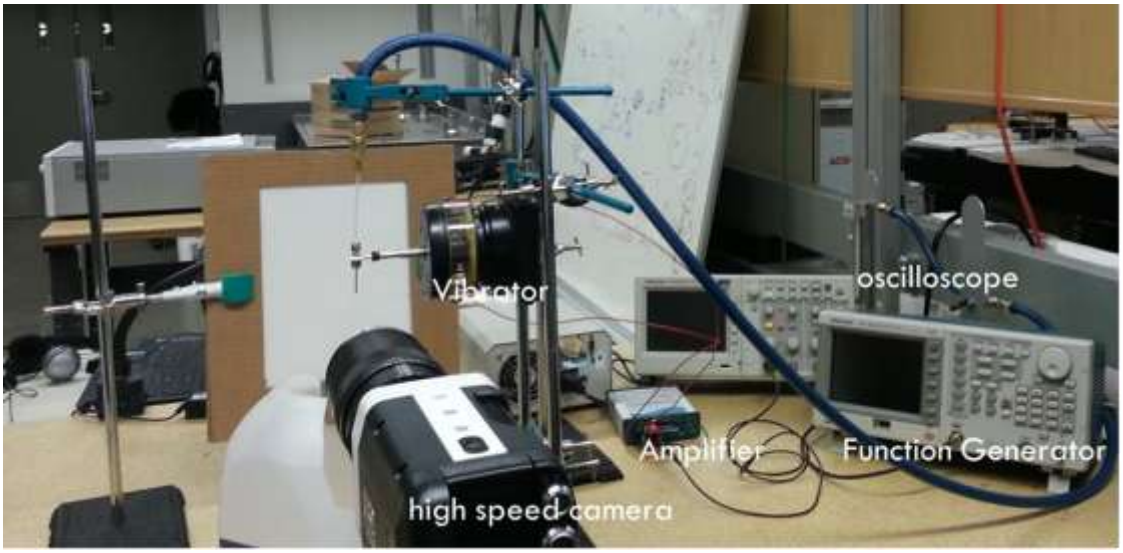

Figure 2-7: Experimental setup for the capillary jet breakup experiment

Table 2-1: Fluid properties

ρ_l	$997\ kg/m^3$
ρ_g	$1.18\ kg/m^3$
μ_l	$9 \times 10^{-4}\ kg/ms.$
μ_g	$1.85 \times 10^{-5}\ kg/ms.$
σ	$0.073\ N/m$

In the experiment, distilled water is used to fill the tank. The gear pump (Cole-Parmer 75211-10) with PDMS (permanent-magnet, direct-current) motor pressurizes water at a desired

pressure and adjusts the flow rate. In addition, the water flow rate is controlled by a flow control valve along with a pressure regulator. Water and air are used as a liquid jet and a surrounding gas, respectively. The fluid properties are listed in Table 2-1 at $25^{\circ}C$.

The presented results are obtained by nozzle with inner diameter equal to 0.25 mm. To analyze the experimental images captured by high speed camera, the outer diameter of nozzle, which is 1/16 inch, is used to set the measuring scale.

The experimental results for development of growth rate of disturbance in the capillary jet are analyzed considering the linear instability assumption. Therefore, the disturbance growth rate is measured similar to the numerical results.

2.4 Imposed Disturbance

As shown in Figure 2-8, there are two types of disturbances, for which the azimuthal mode m=0. A jet subject to the axisymmetric disturbance maintains a straight center line, while the asymmetric disturbance causes the centerline of the jet to be sinusoidal. For jets with low velocities which are in Rayleigh regime, the surface tension force has a stabilizing effect on asymmetric disturbances. Asymmetric disturbance becomes unstable when the aerodynamic interaction between the jet and ambient air is significant. For liquid jets in quiescent air, the significance of aerodynamic force can be determined using the relation provided in Table 1-1, which separates the Rayleigh regime from first wind-induced regime. The relation provides a critical Weber number (We_c) as a function of density ratio and Ohnesorge number. For the water jets (0.25 mm in diameter) studied in the present work, the critical Weber number which is calculated using Table 1-1 is around 530. For jets with Weber number lower than the critical value, the jets are stable to asymmetric disturbances, and their breakup is only caused by axisymmetric disturbance.

2.4.1 Numerical Disturbance

Breakup occurs as a result of the growth of an initial disturbance driven by surface tension forces. The small disturbance at the interface between liquid and gas grows and the jet breaks up downstream toward lower surface energy. In the current numerical simulations, a small

disturbance is introduced by imposing a small sinusoidal fluctuation with amplitude ξ_0 on the streamwise jet velocity at the orifice exit, which is expressed by

$$U'|_{x=0} = 1 + \xi_0 \sin(\kappa t') \tag{2.28}$$

Here $\kappa = 2\pi af/U_0$ denotes non-dimensional frequency, which also is the non-dimensional wavenumber for the travelling wave formed by the advection of the disturbance. The velocity disturbance in Eq. (2.28) can be converted to an axisymmetric radial disturbance on the jet surface by considering a periodically changed flow rate with a constant jet velocity. Initial velocity disturbance is converted into initial disturbance amplitude of the jet radius (η_0). The initial disturbance amplitude is calculated based on balance equation of liquid jet energy. By applying first order approximation, the energy balance equation gives $\eta_0 = \frac{3}{2}\xi_0$.

2.4.2 Experimental Disturbance

In the experiment, a mechanical oscillator driven by sinusoidal voltage waveform was used to perturb the nozzle. As a result, the jet is sinusoidally disturbed with small amplitude. In our experiment, although asymmetric disturbance is imposed at the nozzle to the liquid jet, the Weber number is much less than critical Weber number. Therefore, the jet does not break due to asymmetric disturbance. The liquid jet fluctuation due to nozzle vibration cause changes in liquid energy and similar to the numerical modeling, an axisymmetric disturbance grows and leads to droplet detachment. Additionally, the oscillation also adds kinetic energy to the flow in a sinusoidal function of time, similar to Eq. (2.28). Hence, for the experimental test, it is the velocity disturbance that drives jet breakup.

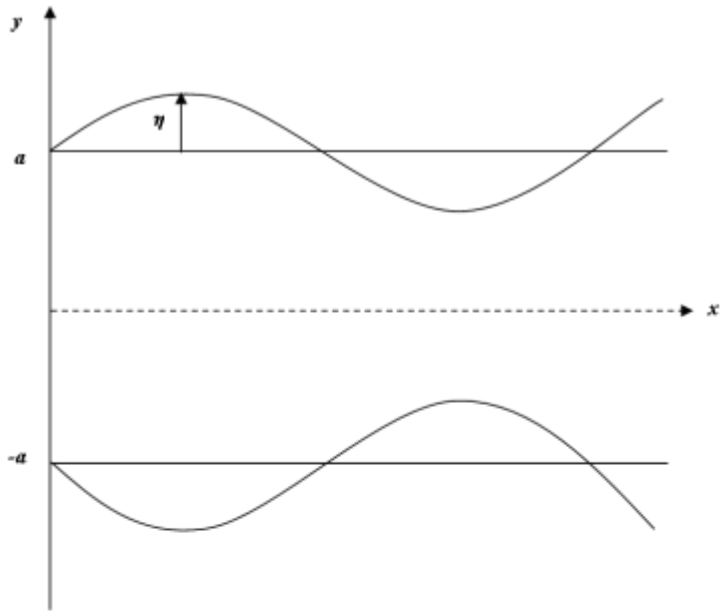

a) Axisymmetrical or varicosal

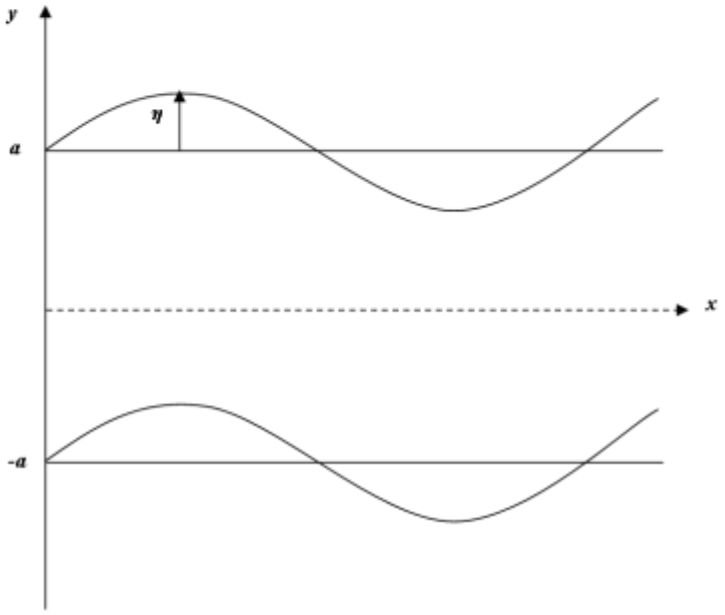

b) Asymmetrical or sinusoidal

Figure 2-8: Axisymmetrical or varicosal (Top) and asymmetrical or sinuousal (Below) periodic disturbances for liquid jet

Chapter 3

Results and Discussion

In this simulation, the breakup of two-phase flow i.e. water and air at ambient temperature, are studied. The breakup occurs due to the amplification of initial disturbance by surface tension forces. The small disturbance at the fluids interface grows and the jet breaks up downstream. In this work, the breakup length, growth rate of disturbance and velocity profile are measured to study the liquid instability of the capillary jet. In addition, a comparison with experimental data is provided to validate the numerical results.

3.1 Breakup Length

A small disturbance is imposed to the fluid right at the nozzle exit. The disturbance continues to grow as the fluid is flowing downstream until a droplet detaches from the continuous jet. The breakup process of a main droplet and its associated satellites detached from the main stream is also presented by the sequence of images in Figure 3-1 and Figure 3-2. Figure 3-1 shows the images in the evolution of a jet simulated by VOF. Figure 3-2 illustrates experimental results to show droplet detachment and its oscillation. In both figures, the satellite droplet has tendency to merge with main stream or droplet. Consecutive images is demonstrated and processed to specify the droplet behavior and its shape after separation. As observed, the oscillation of the detached droplet is damped in to the spherical shape. This progressive relaxation and damping of oscillation is due to viscous dissipation (González & García 2009). These figures also show the time interval between generations of two separate droplets. The production rate of liquid droplets coincides with the frequency of imposed disturbance.

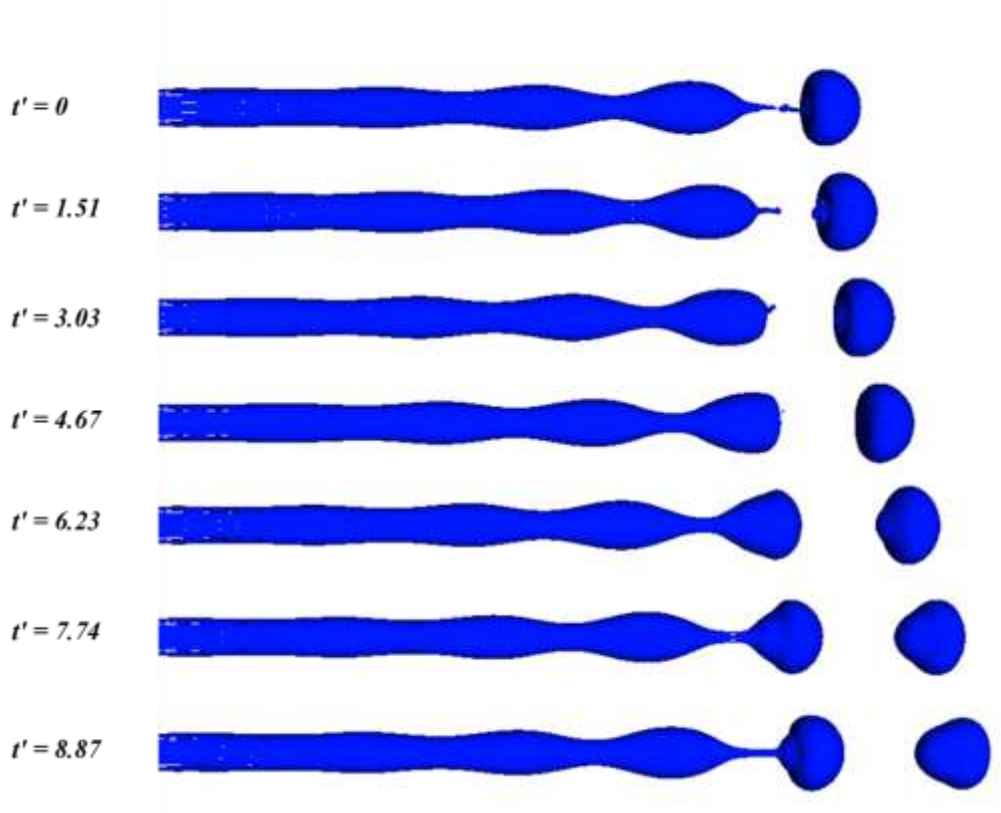

Figure 3-1: Seven instants in the evolution of a jet simulated by VOF illustrating the region where drops have detached from liquid column. An oscillation of droplet is observed after breakup.

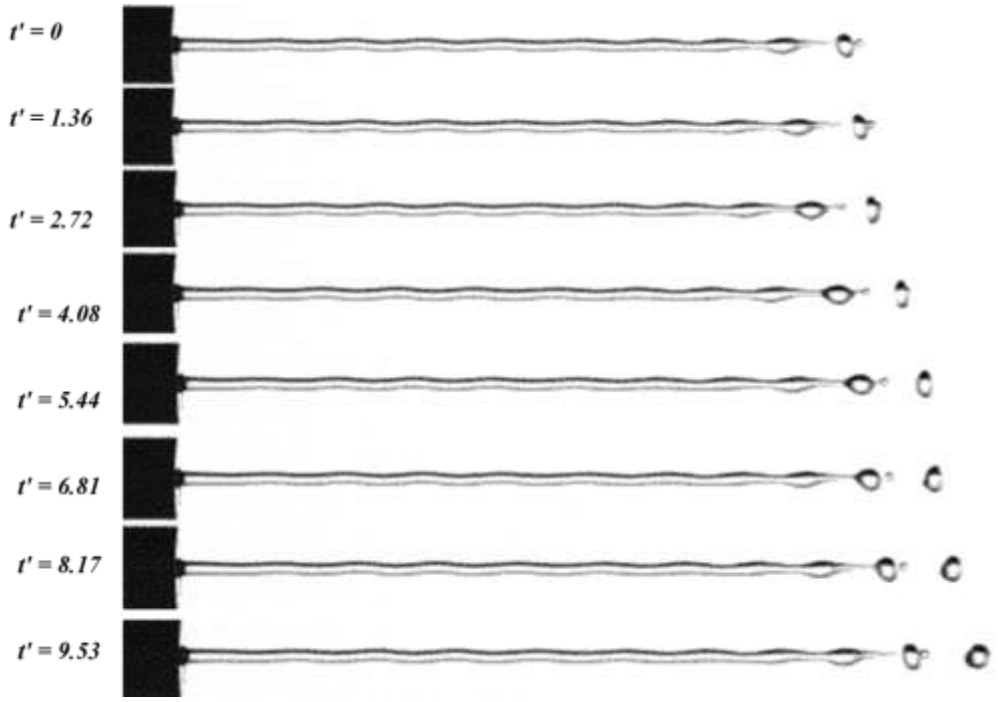

Figure 3-2: Seven instants in the evolution of a jet for experimental results illustrating the region where drops have detached from liquid column. An oscillation of droplet is observed after breakup.

Figure 3-3 shows the numerical results for the breakup of the jet with varied initial disturbance amplitude. As shown, the initial disturbance amplitude has a significant influence on the capillary jet breakup length and drop generation. The breakup length decreases with increasing the disturbance amplitude in the simulation. As shown for the case $\xi_0 = 0$ (unperturbed jet), no disturbance is visible for the first ¾ of the jet length. The disturbance appears near the droplet detachment location. This breakup should be due to growth of numerical noises.

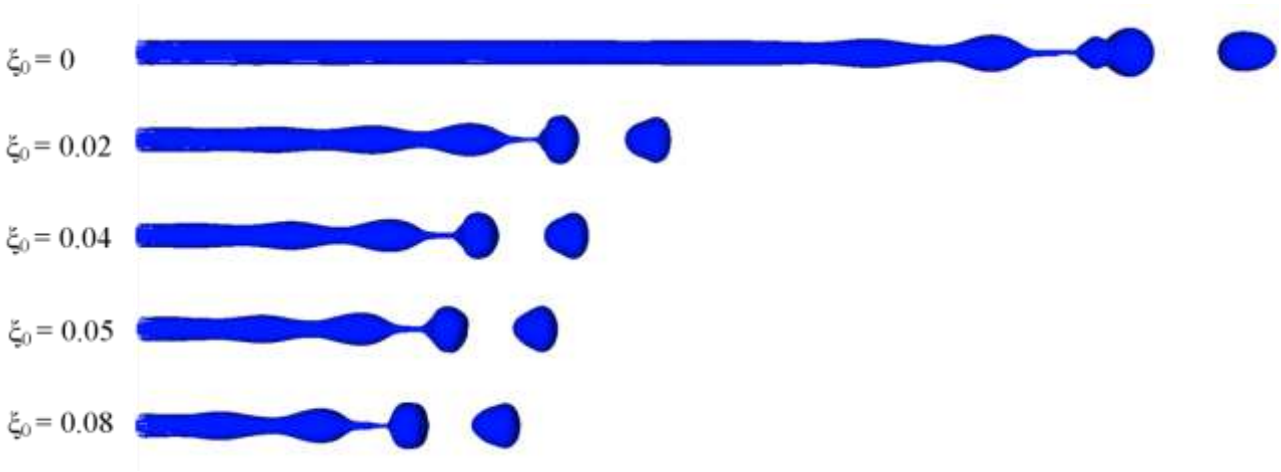

Figure 3-3: Effect of the initial disturbance amplitude on breakup length ($We = 29.6$, $\kappa = 0.7$ and $Re = 840$).

In Figure 3-4, L/L_0 denotes breakup length ratio which is the portion of perturbed jet breakup length (L) to unperturbed one (L_0). The results for numerical modeling reveal that the breakup length is inversely proportional to initial disturbance of amplitudes. So, the breakup length decreases with increasing the disturbance amplitude in the simulation.

The L/D indicates the breakup length measured from nozzle orifice to the tip of broken neck at the time of droplet generation. Figure 3-5 shows L/D for numerical results in comparison with theoretical predictions of Rayleigh theory. Although, the computed breakup length is in good agreement with theory, it is slightly higher than theoretical predictions for higher disturbance amplitudes due to the viscous forces, which are neglected in Rayleigh's theory. The viscosity slows down the growth of disturbance and postpones the jet breakup.

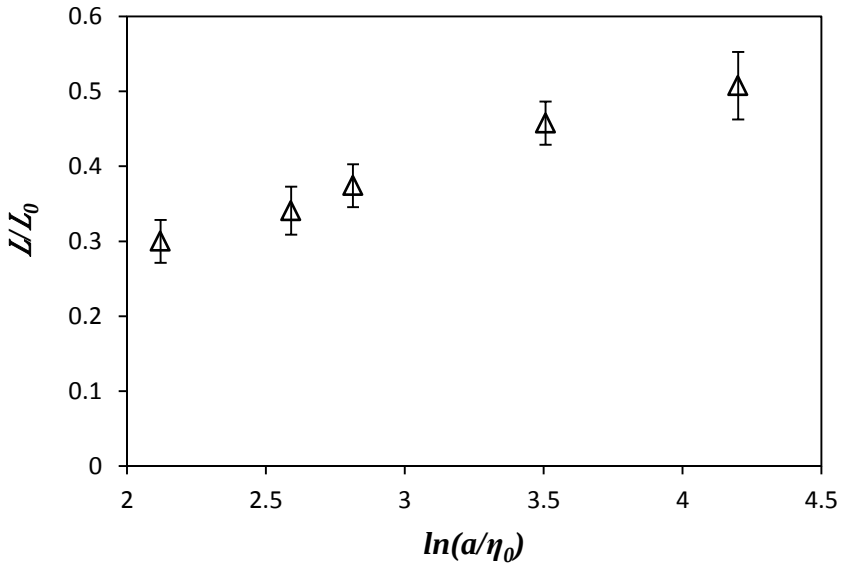

Figure 3-4: Computed numerical results for effect of the initial disturbance amplitude on breakup ratio (L/L_0) ($We = 29.6$, $\kappa = 0.7$ and $Re = 840$).

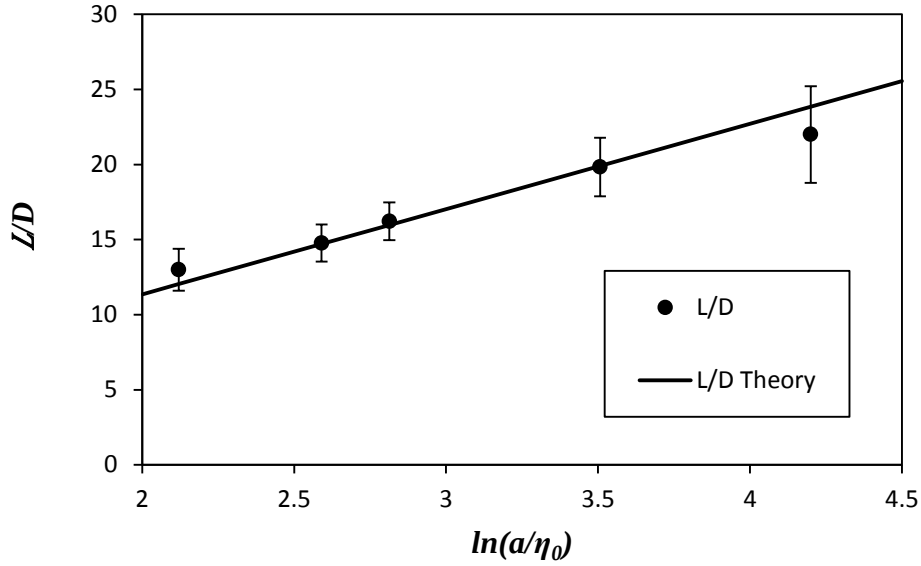

Figure 3-5: Computed numerical results for breakup length to orifice diameter ratio (L/D) with respect to $\ln(\frac{a}{\eta_0})$. ($We = 29.6$, $\kappa = 0.7$ and $Re = 840$).

These findings are also in agreement with those experimental images in Figure 3-6 in which the maximum breakup length is related to unperturbed jet (free jet). For the case of the unperturbed jet, the liquid jet breaks due to some noise from the experimental environment such as setup vibrations or pump velocity fluctuation. For the perturbed cases, by increasing the amplitude of the imposed voltage (E), the reduction of the breakup length is observed. The sizes of generated droplets remain approximately constant as a function of wave length of imposed disturbance. The measured values for reduction of breakup length according to the imposed voltage increases are shown in Figure 3-7.

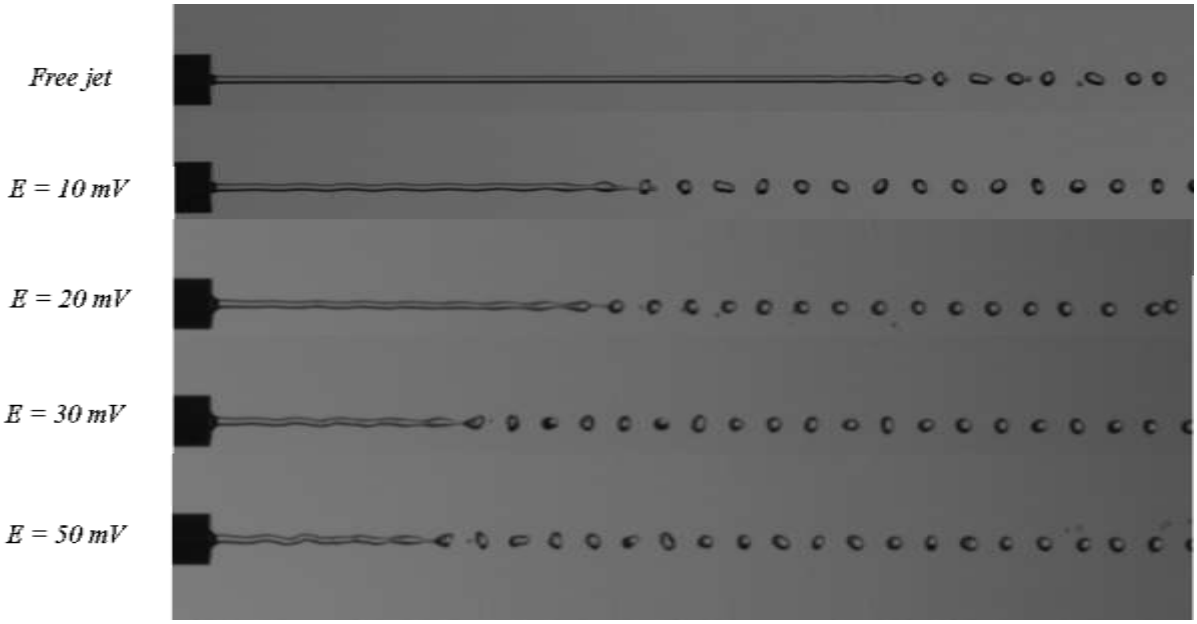

Figure 3-6: Experimental images for effect of the initial disturbance amplitude on breakup length ($We = 29.6$, $\kappa = 0.7$ and $Re = 840$).

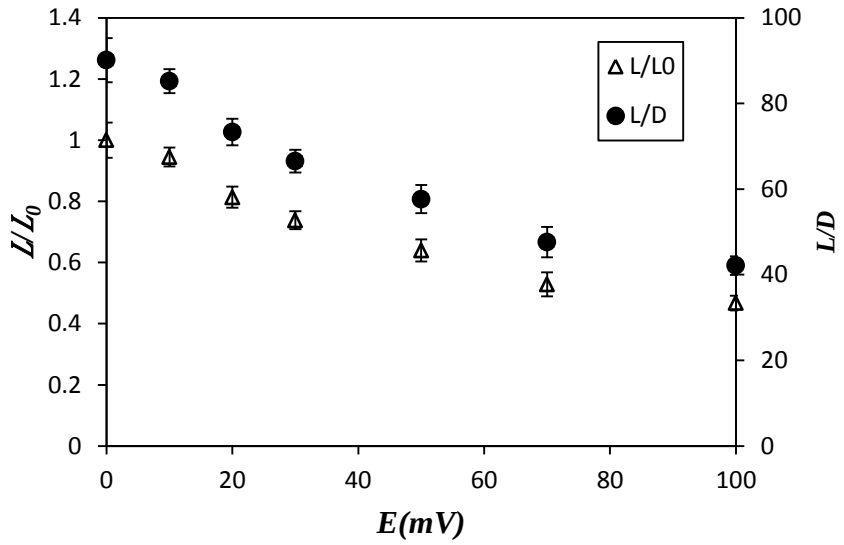

Figure 3-7: Measurment of experimental images for effect of the initial disturbance amplitude on breakup length. Reduction of breakup ratio (L/L_0) and breakup length to orifice diameter ratio (L/D) with respect to applied voltage to the orifice. ($We = 29.6$, $\kappa = 0.7$ and $Re = 840$).

Figure 3-8 and Figure 3-9 illustrate a series of numerical simulations and also experimental images for capillary jet breakup length at different wave numbers. The wave length of disturbance has significant effect on jet breakup. For both numerical simulation and experimental tests, a liquid jet with constant velocity is perturbed with varied frequencies. The breakup mechanism of capillary instability shows quite similar behavior in both numerical and experimental cases. Based on Rayleigh theory, interface disturbance development strongly depends on interfacial wave length. The interfacial wave length should be long enough to allow capillary pinching force sufficiently overcome the restoring capillary force. As illustrated in Figure 3-8, the first case, $\kappa = 0$, shows the breakup length for the unperturbed jet. The breakup of unperturbed jets is due to natural disturbances which are setup vibration or jet velocity fluctuations. By imposing disturbance ($\kappa > 0$), the breakup length decreases until $\kappa = 0.7$. As predicted from Rayleigh theory, for both experimental and

numerical cases, the most unstable wave occurs at $\kappa = 0.7$. For shorter waves with $\kappa > 0.7$, the results show an increase in breakup length. The breakup length for $\kappa = 1$, which is cut-off wavenumber for Rayleigh theory, is almost equivalent to the unperturbed jet.

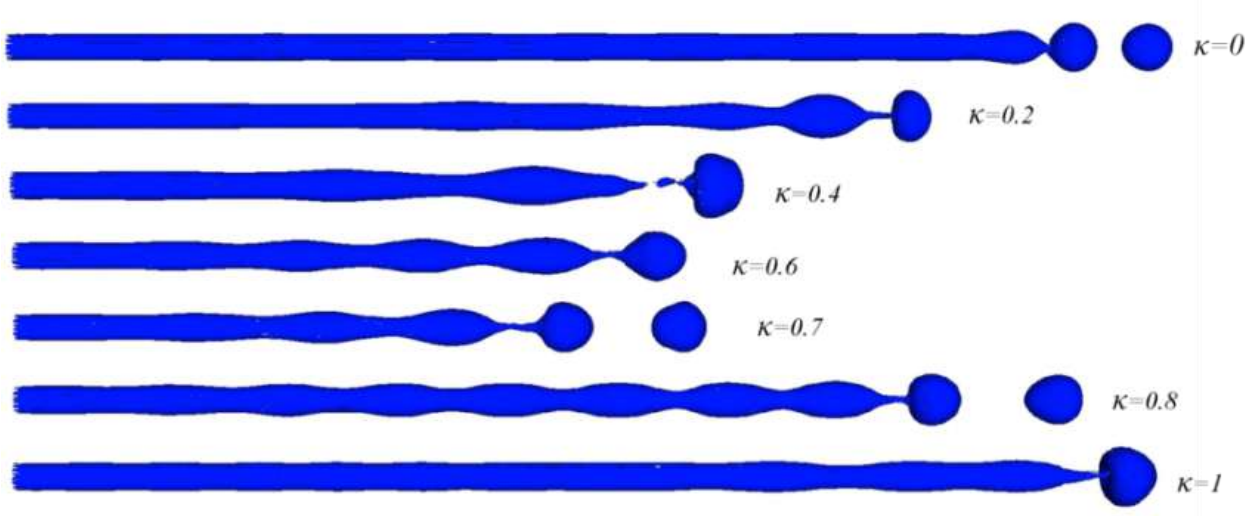

Figure 3-8: Numerical simulation for capillary jets disturbed with varied non-dimensional wave number (κ) ($We = 29.6$, and $Re = 840$).

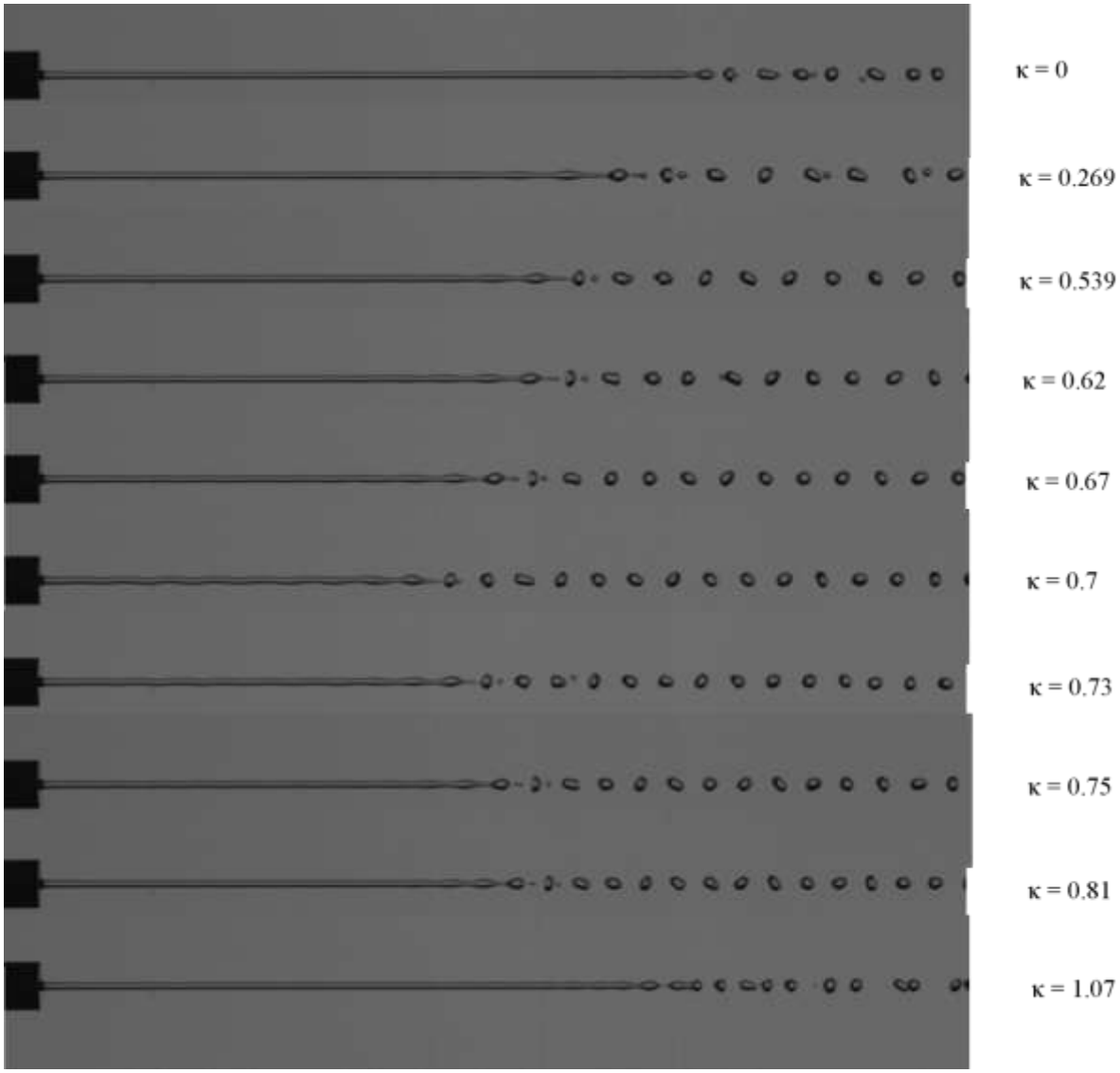

Figure 3-9: Experimental results for breakup length of capillary jet for different nondimensional wave number (κ) ($We = 29.6$, and $Re = 840$).

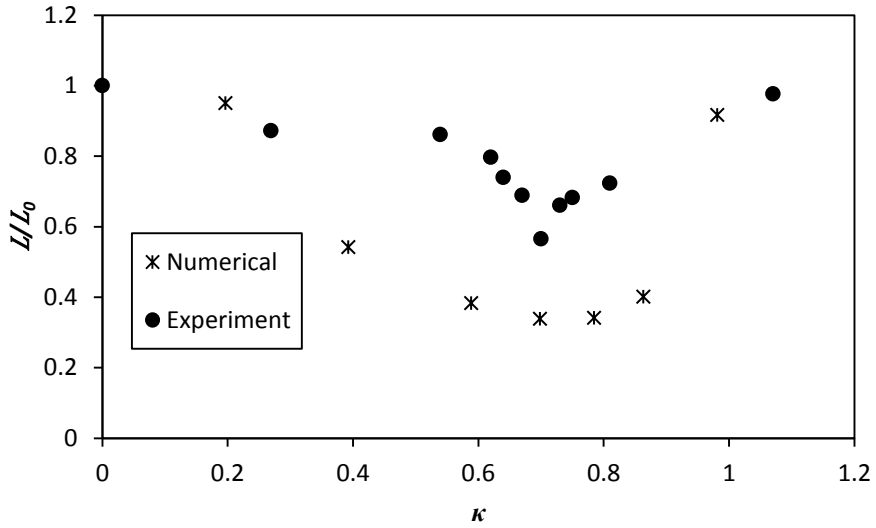

Figure 3-10: Breakup length ratio for numerical simulation in comparison with experimental results with $We = 29.6$ and $Re = 840$.

Figure 3-3 to Figure 3-9 also show that imposing disturbances with wave number $\kappa < 1$ has clear influence on breakup length. The breakup length is reduced due to the imposed disturbances at this range. To clarify the effect of the imposed disturbances with respect to wave number, the ratio of the breakup length of disturbed jet to undisturbed jet is shown in Figure 3-10.

According to Figure 3-10, the minimum breakup length ratio occurs when $\kappa = 0.7$. It is also observed that for shorter waves with $(\kappa \geq 1)$, the breakup length ratio is close to the undisturbed jet. This clearly indicates that disturbances with short wavelength do not assist jet breakup and the jet breaks due to the disturbances of natural noises with long wavelength. The breakup length ratios (L/L_0) for numerical jets are lower than those of experimental jets (see Figure 3-10). The discrepancy between numerical and experimental breakup length ratio should be due to the difference in imposed disturbances to the liquid jet. It should be noted that although the VOF method can measure the imposed disturbance properly, it is difficult to measure it by experiment due to the image resolution. Moreover, it is not easy to minimize

the vibrational disturbance from experimental setup. Therefore, lower breakup ratio seen in the numerical simulations is due to the fact that truncation errors of Gerris are lower than natural disturbances noises from experimental setup.

The dominant regime of jet disintegration is related to the relative velocity between phases. First, Grant et al. (1966) claimed that the jet instability could be described by the response of the coherent part of the jet or the influence of jet velocity on breakup length. Figure 3-11 shows the breakup length of the jet at its most unstable mode ($\kappa = 0.7$) in different Weber numbers. As predicted, the breakup length increases as long as the dominant regime is Rayleigh regime. The growth of breakup length has been continued by increasing the jet velocity up to critical point when aerodynamic forces are high enough to overcome capillary forces and dominant regime changes into first wind induced regime (see Figure 1-6).

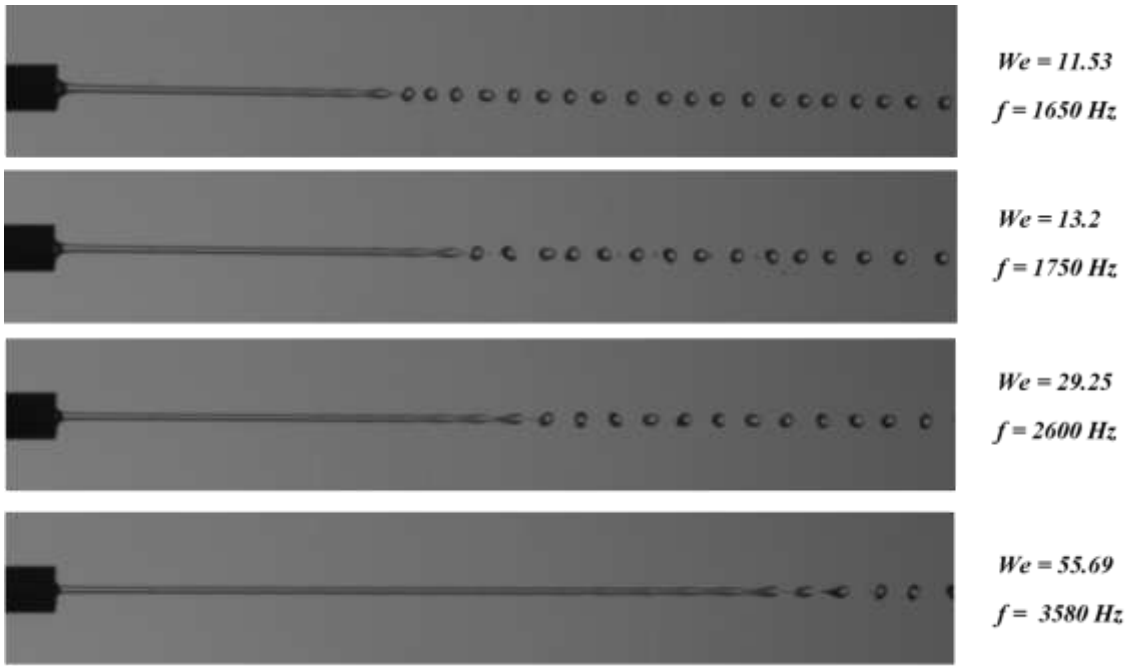

Figure 3-11: Breakup length of the jet at the most amplified instability ($\kappa = 0.7$) at different Weber numbers

According to Table 1-1 and Table 2-1 for spray of water in the ambient air, the dominant regime for $We < 509$ should be Rayleigh mode and breakup occurs with negligible effect from aerodynamic forces. Figure 3-12 represents the variation of breakup length for different jet velocities ($\sqrt{We}$ is proportional to the liquid jet velocity). Theoretical results from linear analysis (Eq. 1.7) are also shown to compare with the numerical data. As shown, by increasing the jet velocity, the breakup length becomes longer and grows linearly because the Rayleigh regime is dominant for $\sqrt{We} < 10$.

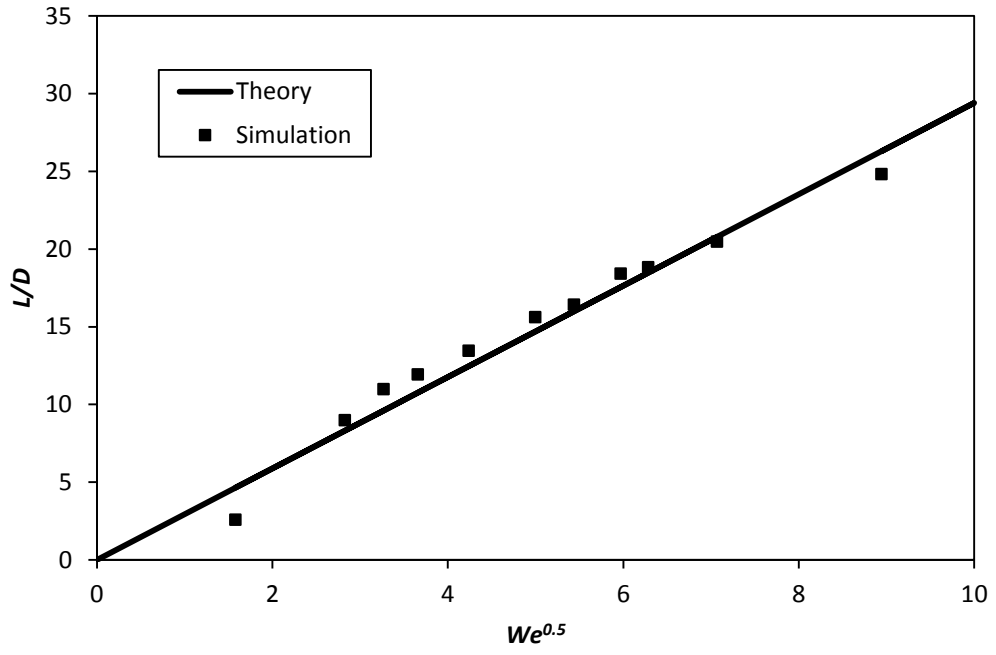

Figure 3-12: Breakup length of the jet at the most amplified instability ($\kappa = 0.7$) for different inlet jet velocities ($\xi_0 = 0.04$)

3.2 Capillary Growth Rate of Disturbance

The numerical results for simulation of capillary jet growth rate are shown in Figure 3-13 to Figure 3-19. As the initial imposed disturbance travels downstream with the jet flow, the jet exhibits periodically spaced swelling and necking zones. The continuous development of swelling and necking zones eventually lead to the generation of free droplets. Also, the volume of each droplet consists of one swelling (where the jet radius increases) and one necking (where liquid jet thickness becomes thinner) zone. Figure 3-13 shows the growth of liquid/gas interface in the swelling zone while Figure 3-14 represents reduction of liquid jet thickness in the necking zone. Results are compared with growth of radius from Rayleigh theory (Eq. 1.10).

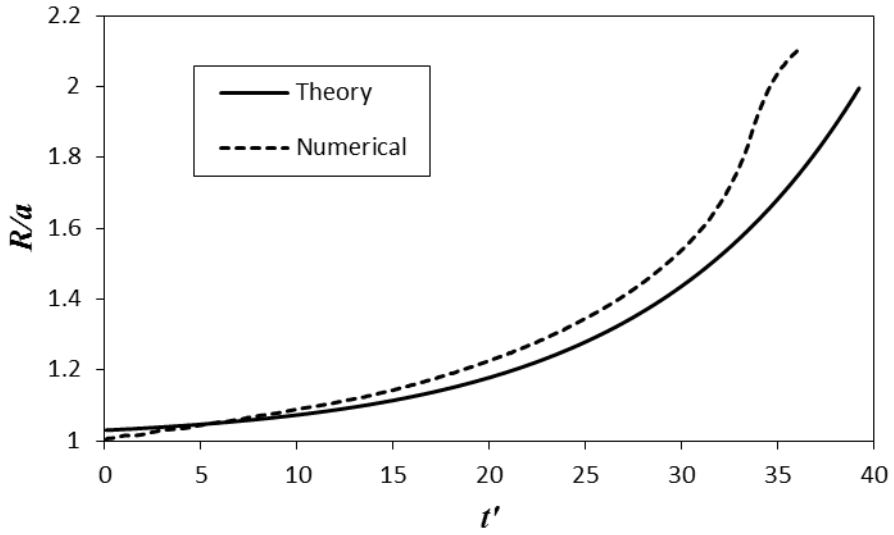

Figure 3-13: Numerical simulation for growth of liquid jet interface in the swelling zone in comparison with theoretical results from Rayleigh theory ($\kappa = 0.7$ and $\xi_0 = 0.02$)

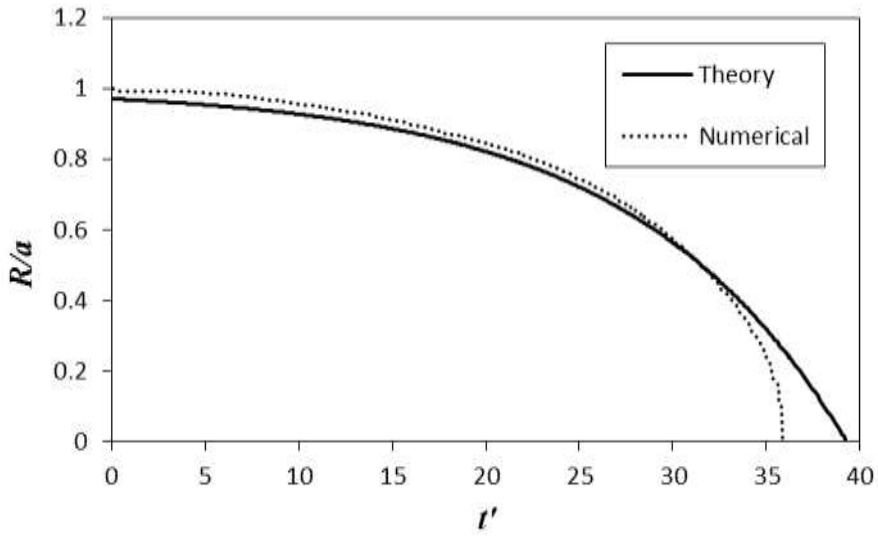

Figure 3-14: Numerical simulation for reduction of jet diameter in the necking zone before jet breakup in comparison with theoretical results from Rayleigh theory ($\kappa = 0.7$ and $\xi_0 = 0.02$)

According to Rayleigh theory, the growth of the disturbance is an exponential function of time, and the key parameter quantifying the exponential growth is growth rate. In this section, growth rate of disturbance is obtained by measuring the growth of disturbance amplitude at the liquid/gas interface. The corresponding numerical result for growth of interface displacement in the swelling zone is shown in Figure 3-15.

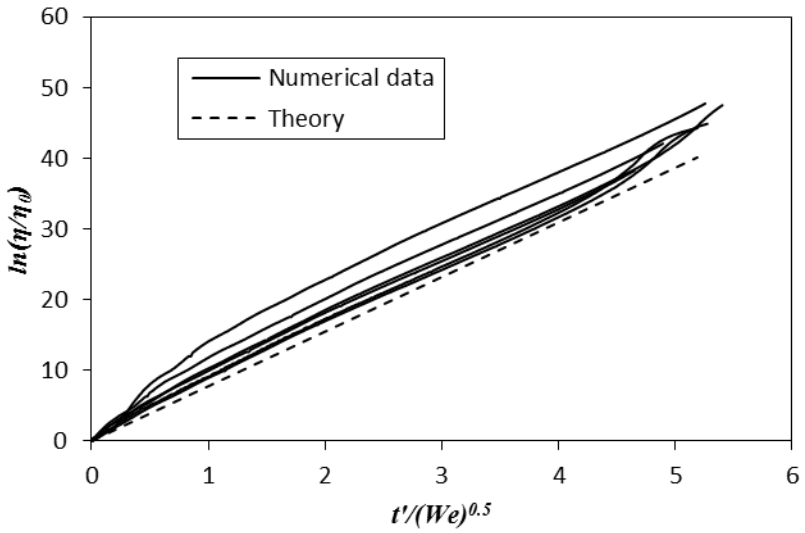

Figure 3-15: Numerical simulation for growth of disturbance at liquid/gas interface for 6 consecutive droplets detachment in comparison with theoretical results from Rayleigh theory with $We = 29.6$, and $Re = 840$.

The interface disturbances with respect to initial disturbance amplitude for detachment of 6 consecutive droplets are shown in Figure 3-15. The natural log of the evolution of interface displacement over initial interface displacement amplitude is plotted as a function of non-dimensional time. The theoretical prediction corresponding to $\kappa = 0.7$ from Rayleigh theory is presented with a dashed line. The slope of the line indicates non-dimensional growth rate, which is capillary time ($\tau = \sqrt{\frac{\rho a^3}{\sigma}}$) times dimensional growth rate (ω). Also, the growth rate is estimated for the detachment of each separate droplet with respect to the development of disturbance. As predicted, the interface position has approximately the same trend with Rayleigh theory. However, the disturbance grows with higher rate near to the nozzle exit and before droplet detachment in the necking zone. This might be the influence of nonlinear effects.

As the disturbance amplitude (η) develops, the growth rate of disturbance is calculated by tracking the interface position of swelling. The growth rate is based on its historical interface growth prior to breakup. By neglecting the nonlinear growth of disturbance at droplet

detachment zone, $\ln(\frac{\eta}{\eta_0})$ develops linearly as a function of non-dimensional time. Therefore, the growth rate for detachment of each separate droplet is estimated as a function of the development of the disturbance amplitude given by,

$$\omega = \frac{\ln(\frac{\eta_{n+1}}{\eta_n})}{t_{n+1} - t_n} \tag{3.1}$$

where η_{n+1} and η_n denote displacement development of one swelling at t_{n+1} and t_n, respectively.

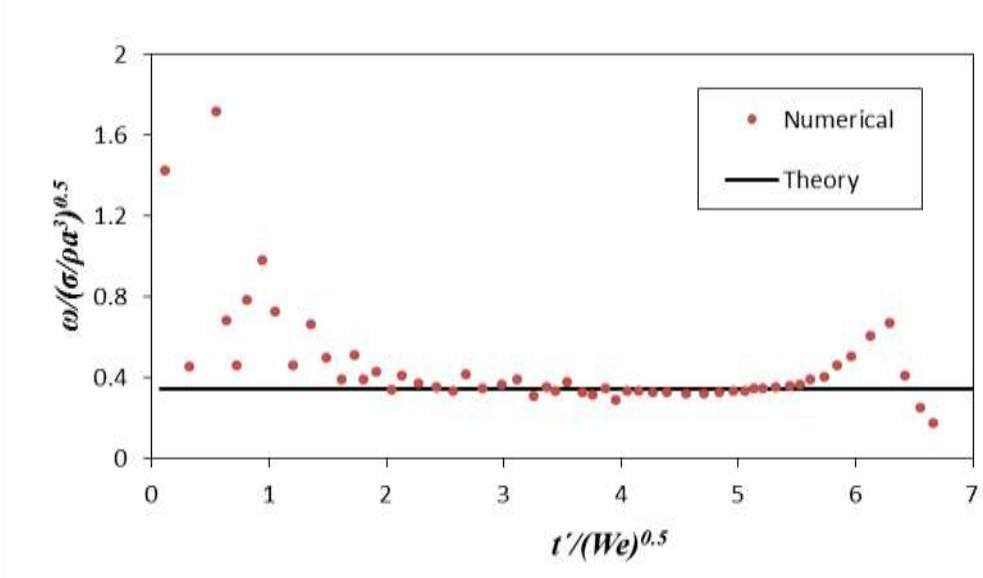

Figure 3-16: Growth rate variation along time. Growth of interface swelling is tracked up to detachment of one droplet ($\kappa = 0.7$)

Figure 3-16 shows the growth rate of disturbance along time for detachment of one droplet. The growth of disturbance is higher than theoretical value near to the nozzle exit but after a while it is slow down and become less than theoretical value. At nozzle exit, velocity difference between liquid and its surrounding gas causes liquid velocity profile change and also growth due to aerodynamic effects. Moreover, higher growth rate before droplet

detachment is due to the increasing of the effects of nonlinear terms which are neglected in linear instability theory of Rayleigh.

It is observed that the growth rates for different droplets are not the same. To compare the numerical results with linear theory of Rayleigh, the average value for growth rate is used. In Figure 3-17, which tracks 10 consecutive droplets, growth rate is reported at the theoretical maximum growth rate ($\kappa = 0.7$) at different times. In this figure, $t = 0$ shows the non-dimensional time for the detachment of the first random droplet. As observed, the value of ω is not constant along time and droplets are generated not always at a constant rate. In other words, time interval between the generations of two droplets is not constant. The corresponding time point is when the droplet detaches from the jet due to the breakup of the neck. The results show that the growth rates fluctuate slightly and the corresponding mean value is less than the Rayleigh theory's prediction. The differences between theoretical growth rate values and those obtained by experiment and also simulation could be due to the effect of jet viscosity and the influence of ambient air which are neglected in Rayleigh theory. Also, the computed breakup length for 14 consecutive droplets shows the same fluctuation (see Figure 3-18). As a result of lower growth rate, the numerical breakup length is slightly longer than that suggested by Rayleigh theory.

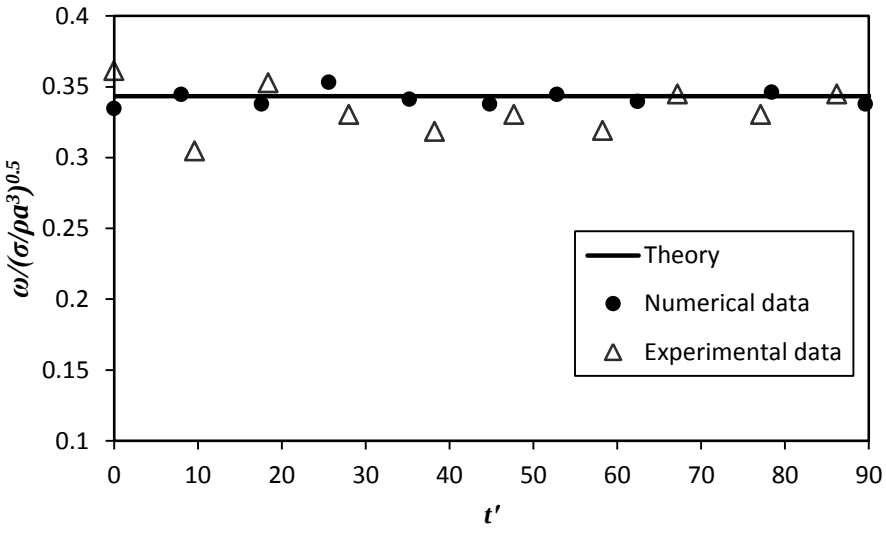

Figure 3-17: Time evolution of growth rate for 10 random consecutive droplets detachment, $\kappa = 0.7$, ($We = 29.6$, and $Re = 840$).

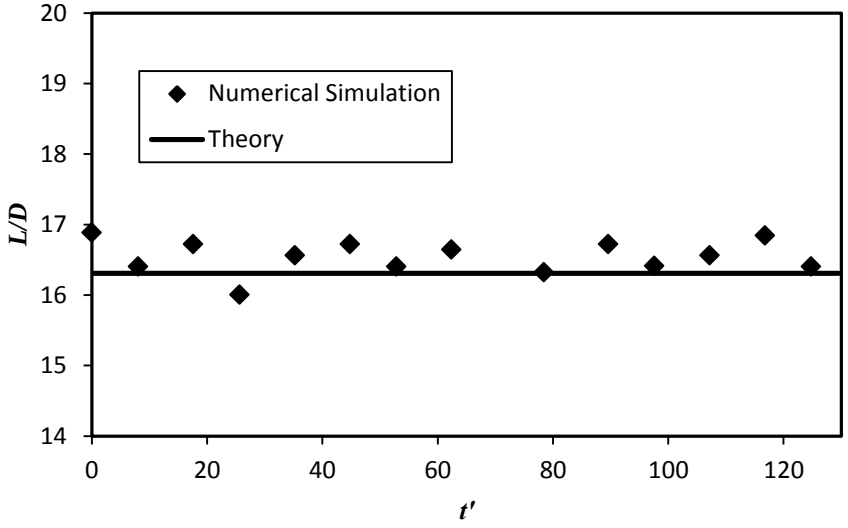

Figure 3-18: Time evolution of growth rate and breakup length for 14 random consecutive droplets detachment, $\kappa = 0.7$, ($We = 29.6$, and $Re = 840$).

Dispersion relation of growth rate of the capillary instability was shown in Figure 3-19 as a function of non-dimensional wave number to compare numerical and experimental results with Rayleigh theory. The growth rate is computed using Eq. (3.1) by tracking the interface and measuring the growth of interface diameter (Simulation-D in Figure 3-19) and also calculated using Eq. (1.14) by breakup time which is estimated by breakup length measurement (Simulation-L in Figure 3-19). The interface tracking would be the best way to measure the interface displacement. As shown in Figure 3-16, the interface grows with approximately constant rate for each separate droplet at $\kappa = 0.7$. The instability behavior at $\kappa = 0.7$ obeys the trend of Rayleigh theory. By increasing the wave length, at lower wave numbers, deviation from linear theory raises. This might be due to the effect of noises which have higher growth rate in comparison with imposed wave number. In these cases, the measuring of growth rate based on breakup time might be a better estimation.

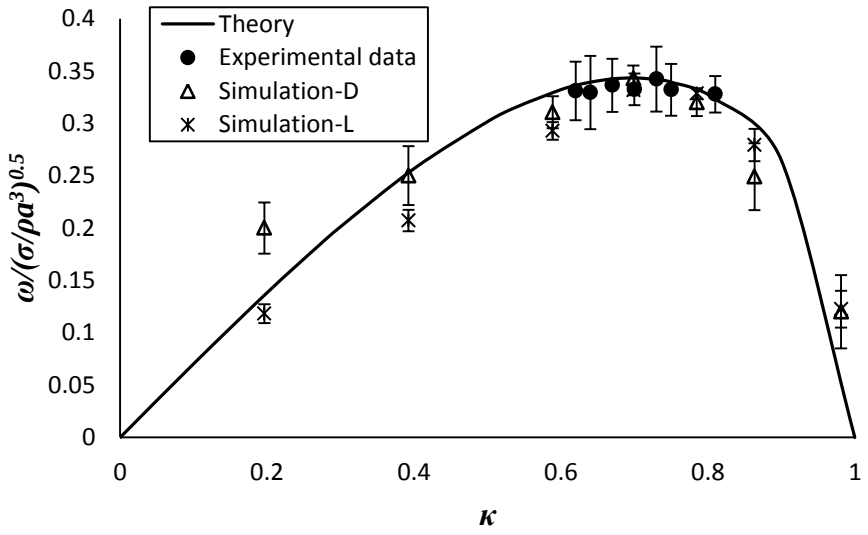

Figure 3-19: Numerical and experimental growth rate in comparison with theoretical one versus wave number with initial disturbance, $\xi_0 = 0.04$, ($We = 29.6$, and $Re = 840$).

3.3 Pressure Gradient and Velocity Profile

In Rayleigh instability theory, the effect of the surrounding gas is neglected. The surrounding gas has an influence on breakup at high jet-gas relative velocities. Because of high curvature in the thinner section of the liquid column, pressure in the necking zone significantly increases (see Figure 3-20). According to the pressure distribution shown in Figure 3-20, a velocity gradient at the necking zone is expected.

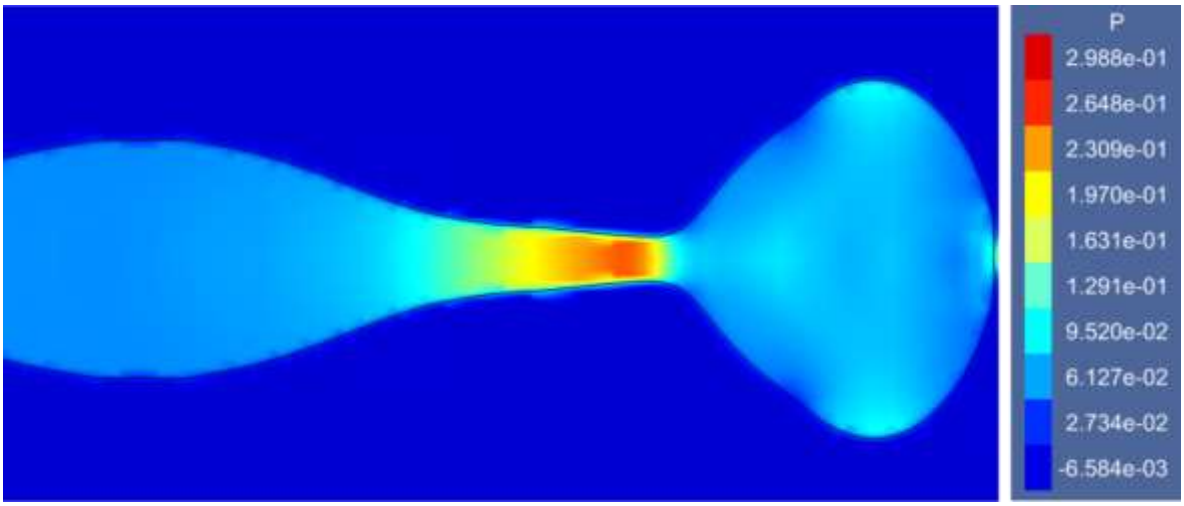

Figure 3-20: Pressure contours of necking zone of jet, $We = 29.6$, and $Re = 840$. Cross section $z = 0$ is shown.

Figure 3-21 shows a series of images exhibiting of pressure distribution variation in the necking zone at different times. In the necking zone, the pressure changes with respect to capillary forces. As observed, development of necking causes changing in the surface curvature, and pressure gradient increases due to higher capillary forces.

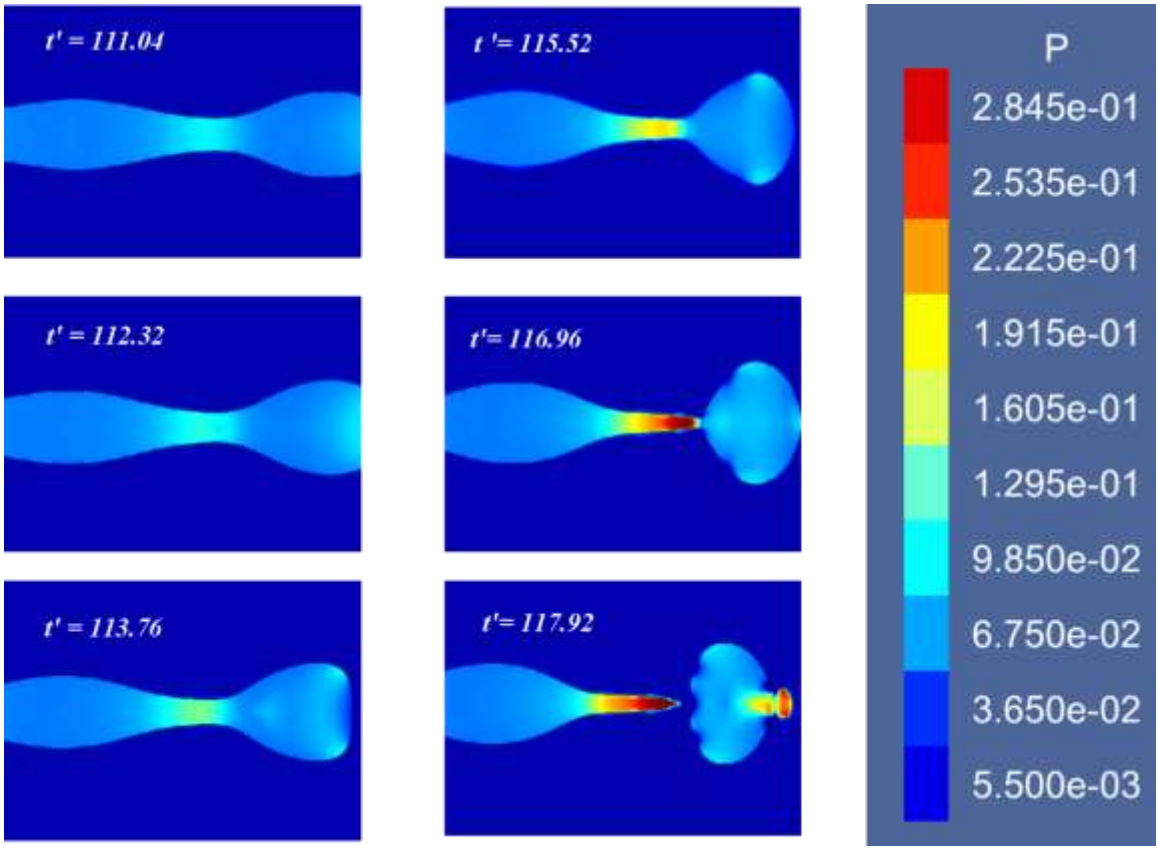

Figure 3-21: Series of images for pressure contour changes of necking zone of jet at different times, $We = 29.6$, and $Re = 840$. Cross section $z = 0$ is shown.

Figure 3-22 demonstrates the liquid jet deformation and representative streamwise velocity contours in the breakup region. Figure 3-23 illustrates the streamwise velocity profiles through the liquid jet core in various positions which were shown in Figure 3-22 with dashed lines. The black circular symbols indicate the liquid/gas interface at each x location. Generally, the central line of the liquid jet has a higher velocity than the gas except for upstream of the necking region. As observed, the liquid centerline velocity is reduced until it reaches to the upstream of necking zone. It should be noted that the initial velocity profile of the jet is uniform. Velocity profile in Figure 3-23 clearly shows that the velocity profile has been affected by the ambient gas. The viscous stress causes reduction of liquid streamwise velocity near liquid/gas interface. This velocity gradient makes the neck thinner until

detachment of droplet occurs. The velocity distribution after the necking zone (x/D=17.6) is approximately similar to the one before this region (x/D=13.6). As shown, the lower liquid jet velocity in comparison with surrounding gas velocity at upstream of necking zone (x/D=15.8) is observed. On the other hand, the downstream liquid velocity (x/D=16.8) is much higher than that of surrounding gas.

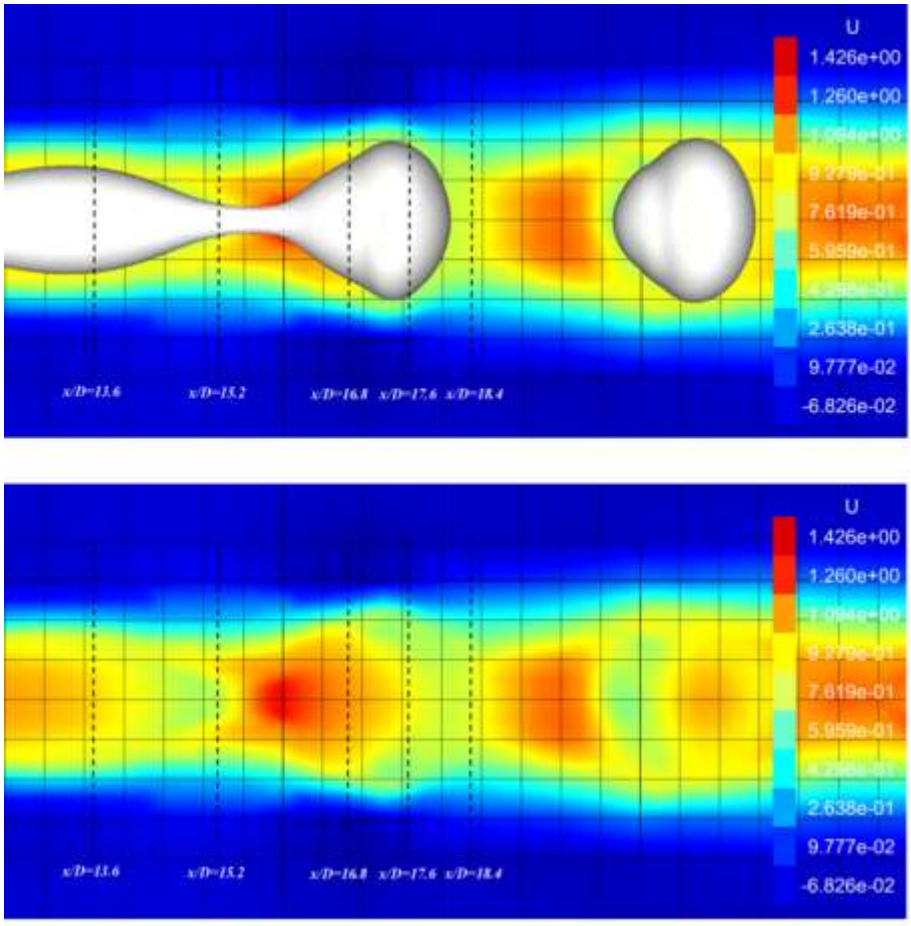

Figure 3-22: Velocity magnitude contours in the breakup region of capillary jet. Cross section $z = 0$ is shown ($t' = 132.74$).

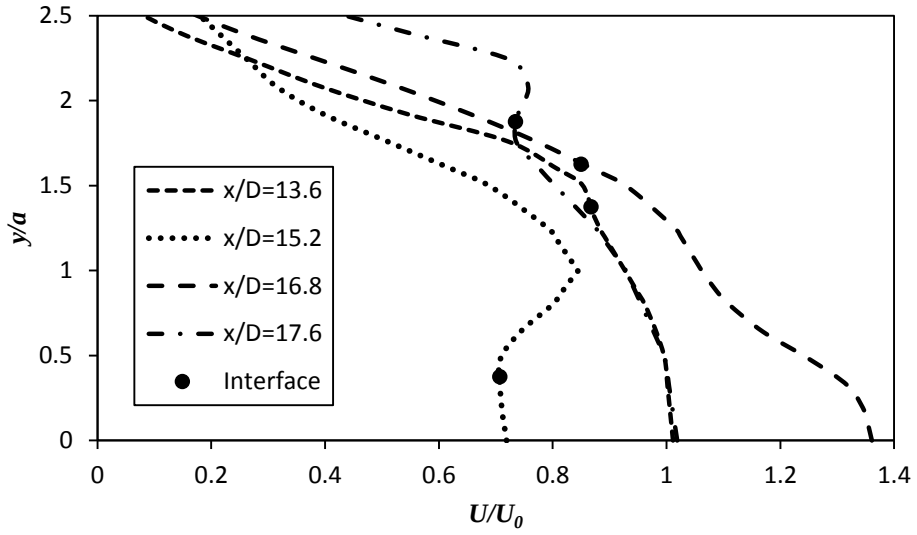

Figure 3-23: Streamwise velocity profile through the liquid jet core and surrounding gas in various positions with initial disturbance, $\xi_0 = 0.04$, $We = 29.6$, and $Re = 840$. Cross section $z = 0$ is shown.

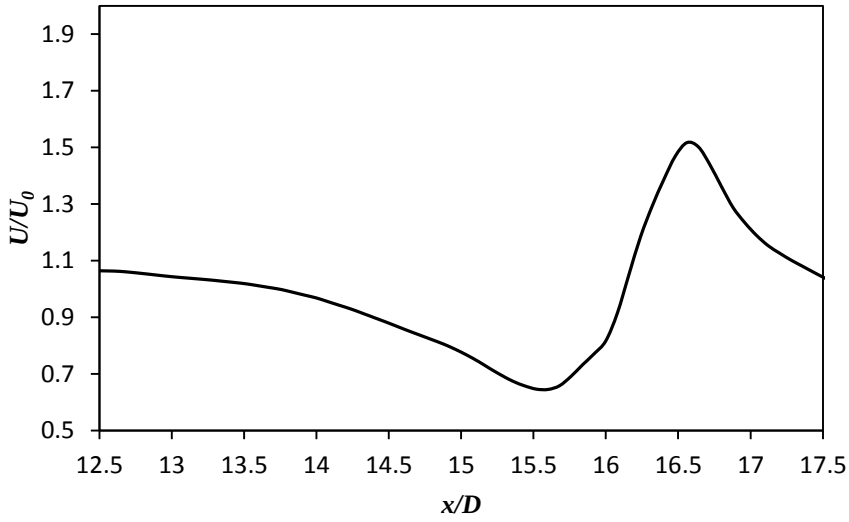

Figure 3-24: Centerline streamwise velocity with initial disturbance, $\xi_0 = 0.04$, $We = 29.6$, and $Re = 840$.

The liquid velocity is increased at downstream of the necking zone and decreased upstream of necking zone due to the high capillary forces. The centerline streamwise velocity is presented in Figure 3-24. As observed, the centerline jet velocity is reduced until upstream of necking zone. Due to the high pressure gradient in the necking region, the centerline velocity increases dramatically up to downstream of necking. The jet velocity is decreased after this region and has tendency to reach mean velocity of the jet.

Figure 3-25 demonstrates the velocity profile changes in the necking zone at the breakup time. The streamwise velocity becomes almost zero for the gas which is far from liquid jet. It is also clear that the velocity at the necking region is in the positive streamwise direction before the detachment of the droplet. Consequently, the high velocity gradient which is also observed in the necking region makes this section thinner than other regions.

At the moment of main droplet detachment, low streamwise velocity in the upstream and high streamwise velocity in the downstream intensifies the velocity gradient (see Figure 3-25b). The initial shape of the detached droplet is dramatically deformed but remains approximately symmetric with respect to the x-axis.

As mentioned, the velocity gradient occurs due to high pressure gradient in the necking zone. Figure 3-26 is plotted to show the centerline liquid jet pressure and to clarify the relation between velocity and pressure gradient in the necking zone. The high pressure of liquid jet in the necking zone (x/D=16) when jet cross section curvature (jet radius) is relatively small and jet axial curvature is high.

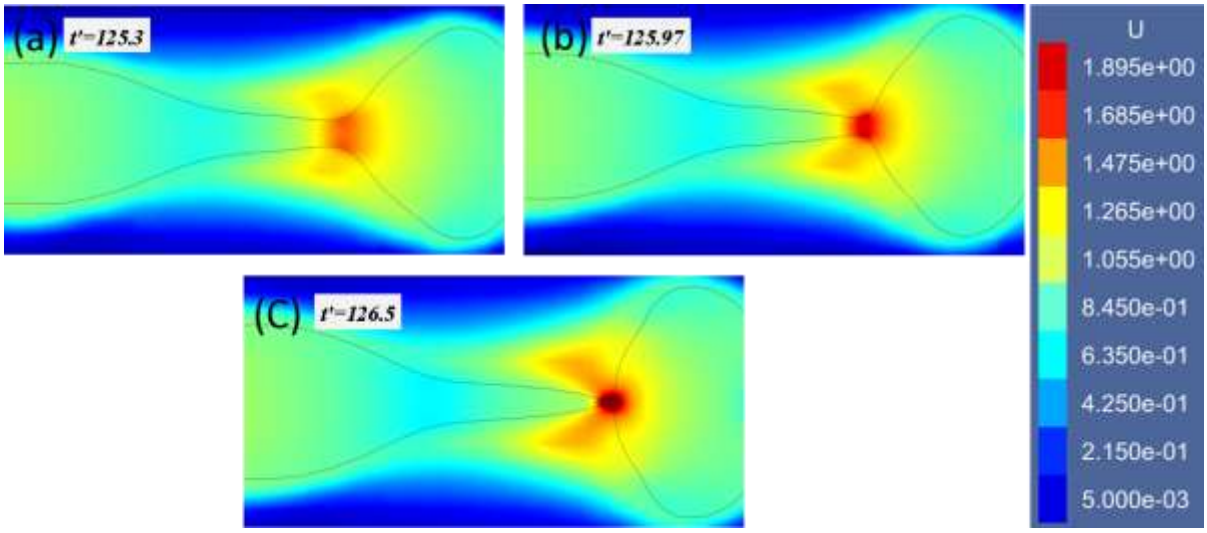

Figure 3-25: (a), (b), and (c) Velocity contour of necking zone at jet breakup time ($We = 29.6$ and $Re = 840$) Cross section $z = 0$ is shown.

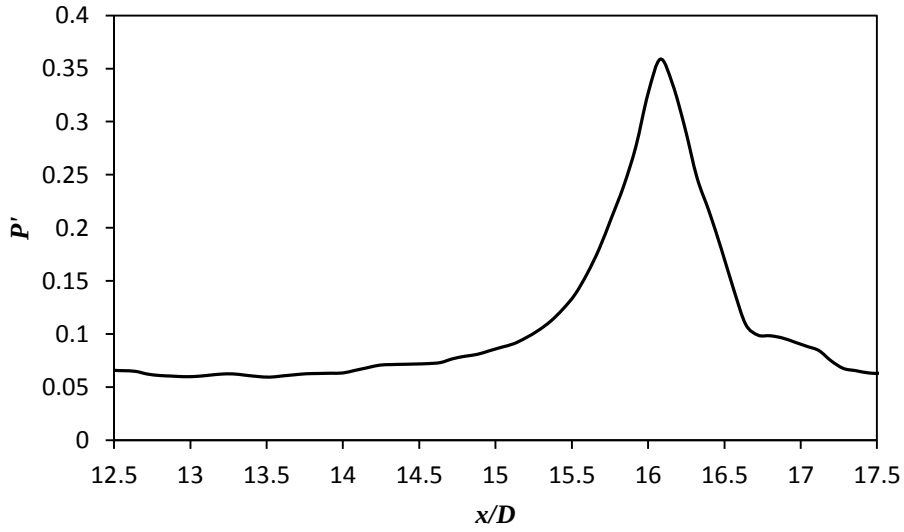

Figure 3-26: Centerline pressure distribution in the necking zone $We = 29.6$, and $Re = 840$ ($t' = 132.74$).

Figure 3-27 shows temporal pressure at a constant point which is located in the middle of necking zone ($x/D = 16$). Each peak in the chart indicates detachment of one droplet. Changes in pressure amplitude indicate variation of necking zone position and its related breakup length. In other words, as droplet detachment point varies, the centerline points corresponding to maximum and minimum centerline pressure are shifted.

In addition, velocity gradient is expected due to high local pressure gradient in necking region. Figure 3-28 shows velocity changes when necking reaches $x/D = 16$. As observed, the velocity increases when downstream of necking region reaches the assigned point. On the other hand, when upstream of necking region reaches assigned point ($x/D = 16$), the streamwise velocity increases.

Figure 3-29 is illustrated in order to describe the physical process that causes pressure and velocity changes at $x/D = 16$. As observed, at $t' = 53.47$, the liquid necking flows toward assigned point ($x/D = 16$). The maximum pressure and velocity appear when the center of the necking zone reaches this point. This figure shows downstream of necking region after breakup at $t' = 56.21$ when pressure is decreasing. Comparison between Figure 3-29 with Figure 3-27 and Figure 3-28 demonstrates that each peak for pressure and velocity gradient represent growth of a necking and detachment of droplet.

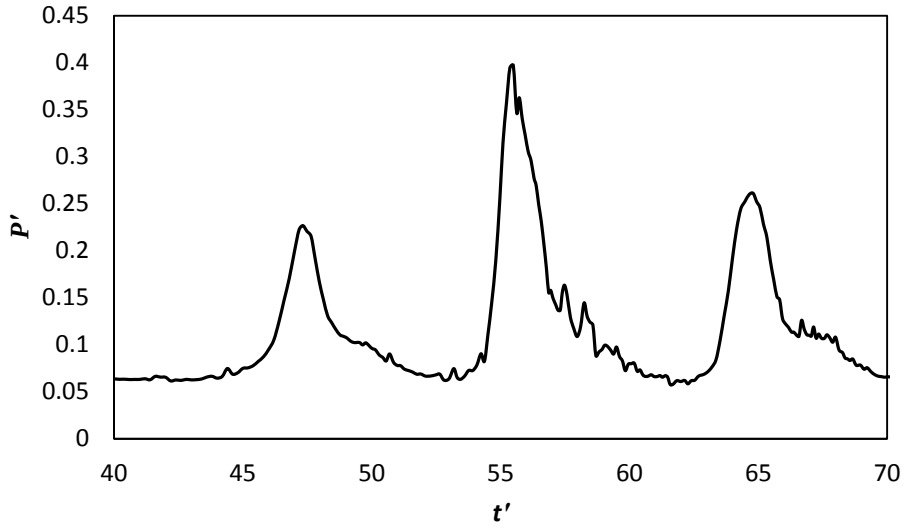

Figure 3-27: Centerline pressure distribution in the necking zone with respect to time for $x/D = 16$, $We = 29.6$, and $Re = 840$.

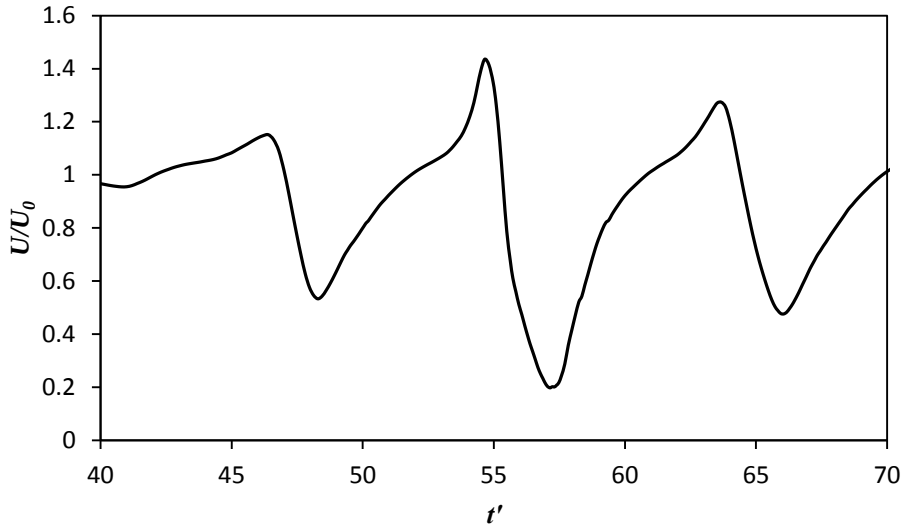

Figure 3-28: Centerline streamwise velocity distribution in the necking zone with respect to time for $x/D = 16$, $We = 29.6$, and $Re = 840$.

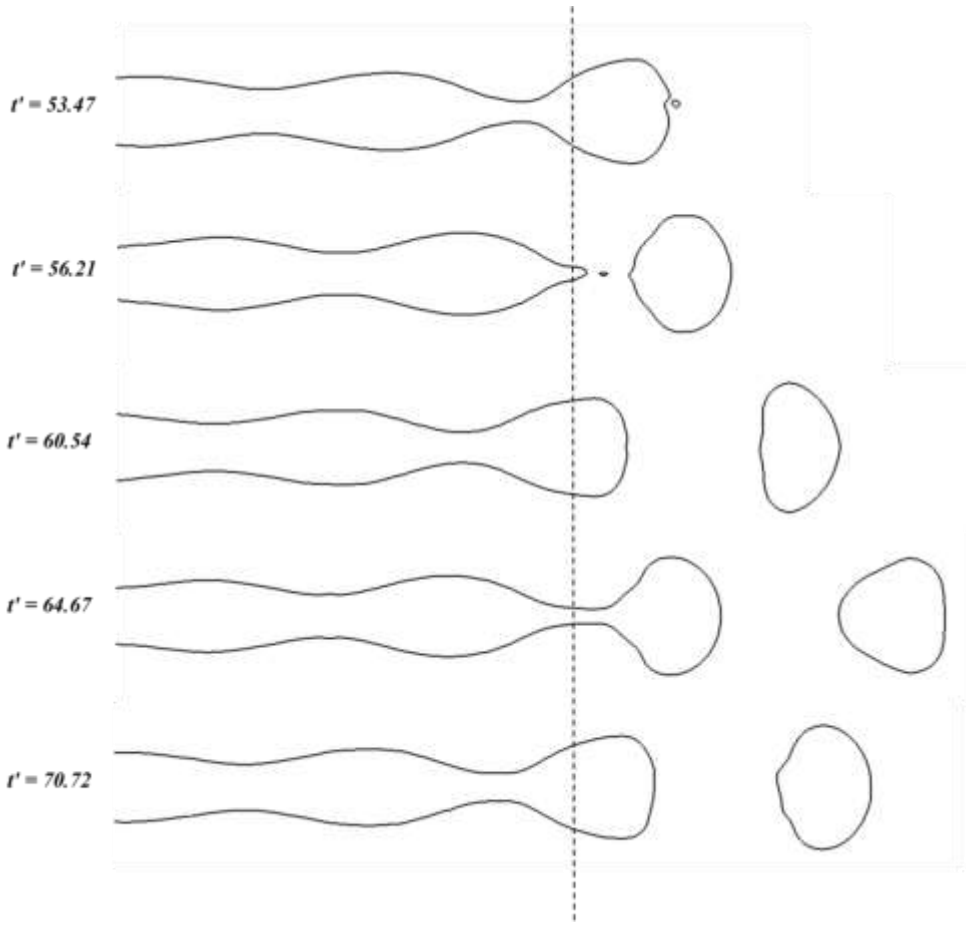

Figure 3-29: Series of images showing the liquid jet at different times at certain position, dashed line shows $x/D = 16$, ($We = 29.6$, and $Re = 840$). Cross section $z = 0$ is shown.

Figure 3-30 shows series of images to illustrate radial velocity. As observed, the high radial velocity for gas appears at necking zone and also around droplet before its formation. Also, after droplet formation, significant air motion is still visible due to detached droplet oscillations.

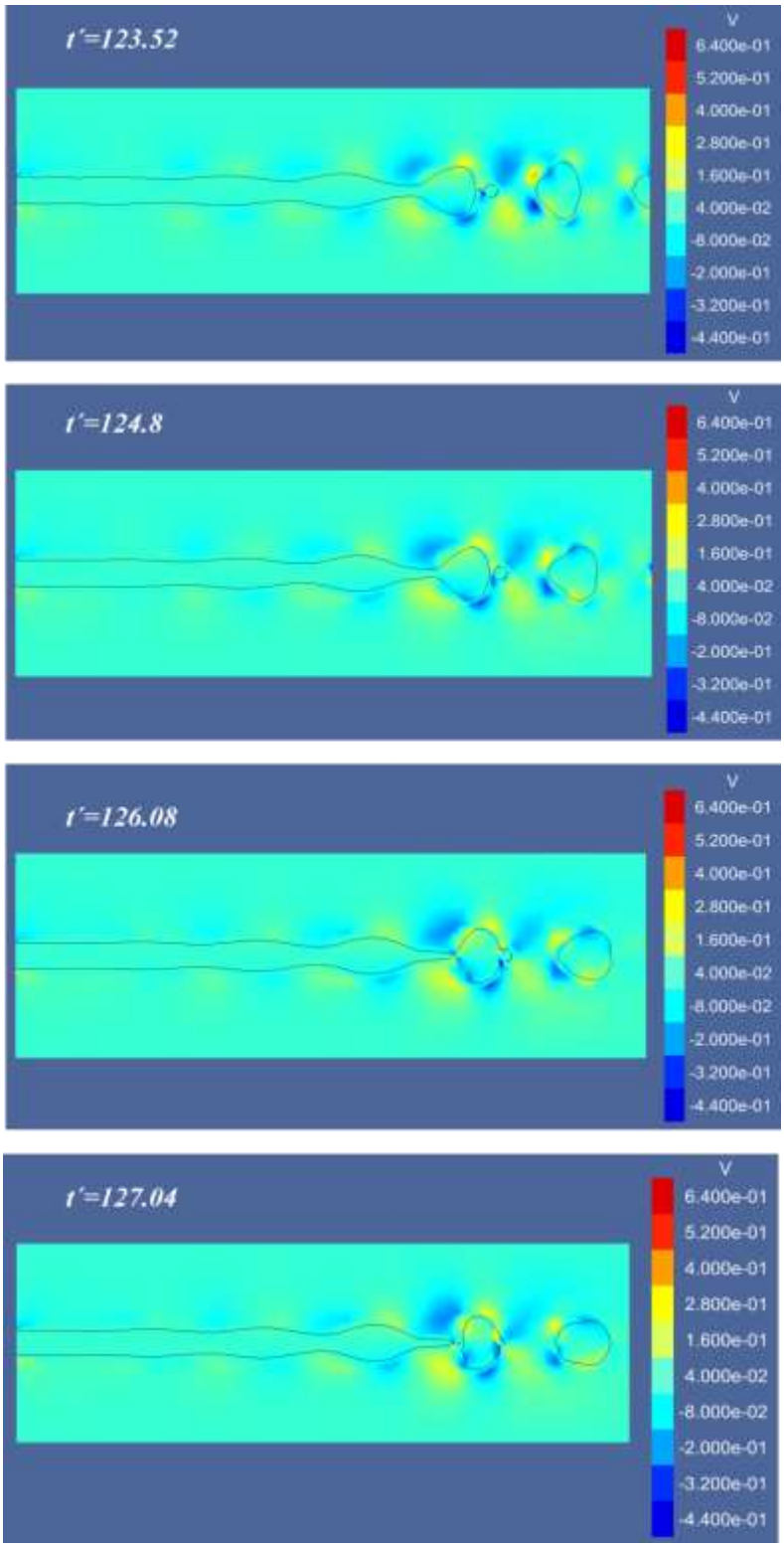

Figure 3-30: Series of images for radial velocity vector at different times ($We = 29.6$, and $Re = 840$). Cross section $z = 0$ is shown.

3.4 Path Lines

The Lagrangian tracking of moving particles with fluid velocity is used to determine liquid path lines. In the Lagrangian method, the coordinates of each fluid particle is described by determining its position vector as a function of time.

As shown in Figure 3-31, four individual fluid particles are considered in the nozzle outlet to plot the trajectory of particle motions. Furthermore, the interface between liquid and gas is specified with a dashed line to point out its growth. The results show the path lines remain symmetric with respect to the streamwise component of flow. It is also observed that the interfacial particles do not necessarily remain at the maximum of the swelling part. The particle which is close to the interface initially moved inside the liquid jet due to its lower velocity and traveled toward the necking zone. In other words, these particles were replaced with some particles which were initially located in the middle of the liquid jet.

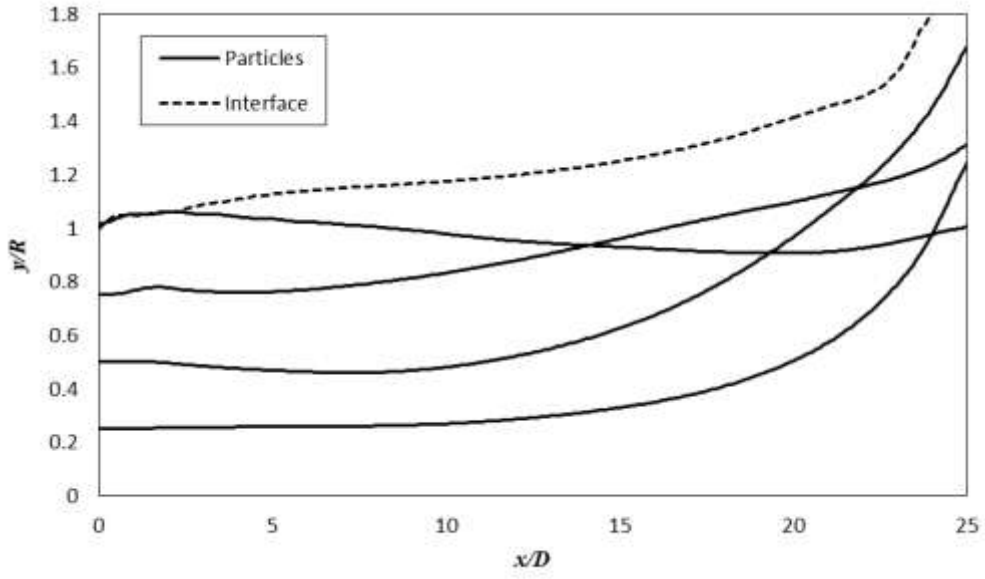

Figure 3-31: Flow path-lines of tracers released at the jet inlet. Continous lines show the path of particles inside the jet. Dashed line indicate the path for tracer which is located at the interface and tracks position of interface for swelling until droplet detachment.

Figure 3-32 shows a series of images to demonstrate the particle locations inside the jet at different times. As shown, the particles are marked with different colors to be recognizable. The red color indicates the particle which is close to interface initially. As the jet release into air, high velocity profile change appears in the liquid jet. Therefore, the particle near to the interface (red particle) which has lower velocity moves slower than inner particles (blue, green, and black particles). It is also observed that the red particle moved toward upcoming necking zone and the swelling part was filled out with the central ones.

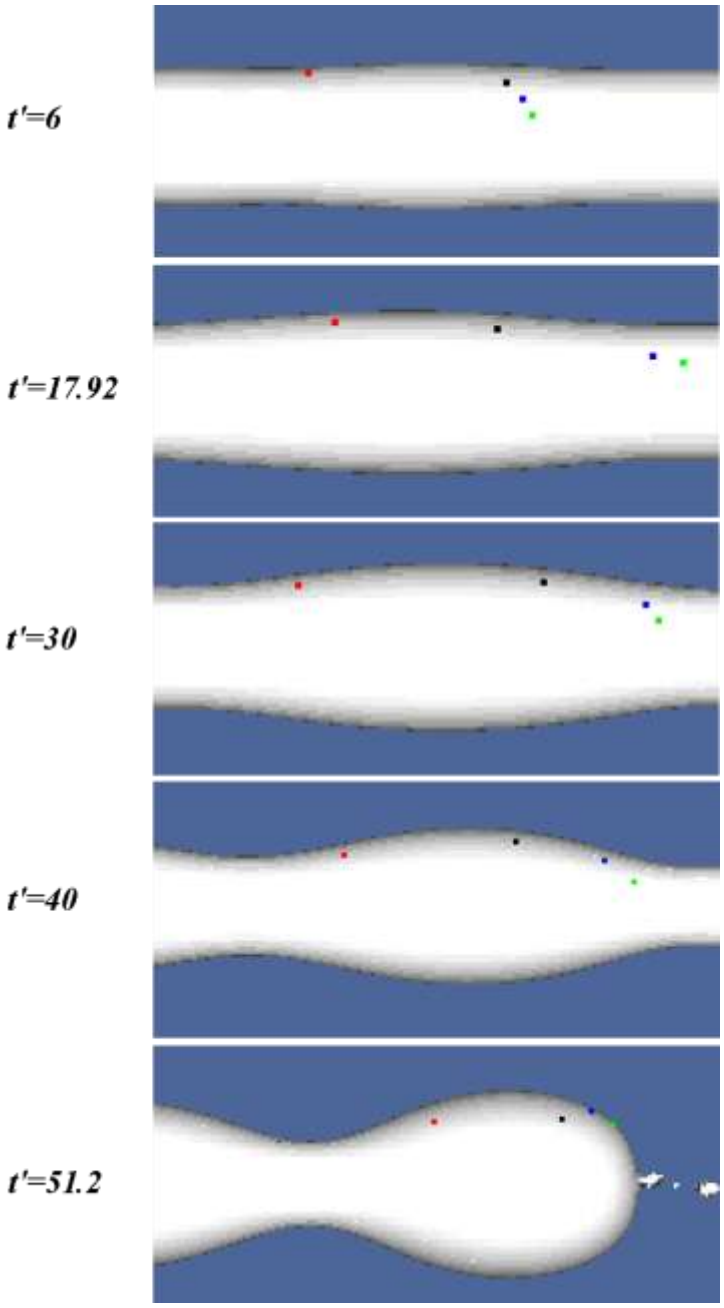

Figure 3-32: Series of images for movement of liquid particles considered inside liquid jet at different times ($We = 29.6$, and $Re = 840$) Cross section $z = 0$ is shown.

Chapter 4

Conclusion and Future Work

4.1 Conclusion

This work presents a numerical simulation for liquid jet instability and its breakup in comparison with experimental data and theoretical predictions. The simulations based on Volume of Fluid (VOF) method were performed to capture the liquid/gas interface with the open-source code "Gerris", capable of adaptive octree grading.

The breakup length and growth rate of disturbance are computed under the assumption of a sinusoidal velocity disturbance at the nozzle exit. To confirm the validity of results, the numerical data are compared with the experimental images captured by high speed photography. The interfacial development of the jet radius is used to calculate the growth rate of disturbance. On the other hand, the velocity profile and path lines are illustrated to explain droplet detachment due to capillary forces and its effect on fluid particles moving inside the jet.

The breakup length and growth rate of disturbance are examined for a different range of wave numbers. Both numerical and experimental data indicate that the maximum growth rate which causes the shortest breakup length occurs around $\kappa = 0.7$. For short waves ($\kappa > 1$), jet might break due to dominant natural disturbances and the measured breakup length is similar to unperturbed jet breakup length.

Although aerodynamic forces are negligible at Rayleigh regime, the numerical results and experimental data for breakup length show the effect of viscosity and aerodynamic forces even at low velocities. The velocity profile of the jet is clear evidence showing the effect of aerodynamics. Due to aerodynamics effects, the uniform initial velocity changes and velocity gradient appears in the liquid jet. High centerline jet velocity causes faster movement for central liquid particles comparing with interfacial ones. As observed from Lagrangian particle approach, particles near the centerline have tendency to move toward interface due to their radial velocity and fill out the swelling part. On the other hand, interface particle comes

toward center and moves to the upcoming necking region. Therefore, development of swelling and necking zones appears.

4.2 Future Work

- Natural disturbances or noises due to instrument vibration or pump velocity fluctuation occur in several industrial applications. However, droplet production rate, size of droplet and jet breakup length and angle are some parameters that have significant variation particularly at high disturbance amplitudes and frequencies (see Figure 4-1 and Figure 4-2). Therefore, study of capillary jet instability with high disturbance amplitude (longer than jet radius) for wide range of frequencies is suggested as a future work.
- Jet breakup and liquid instability have several industrial applications, especially at high velocities when turbulence happens. As a future work, jet breakup and droplet fragmentation at high Weber and Reynolds numbers, when second wind induced or atomization regimes are dominant.
- For the case of capillary jet, we focused on breakup length and growth rate of disturbance. The fragmentation of droplet and their oscillation modes can be investigated as a future work.
- Detachment of satellite droplets are one of the main concern in the jet printing technology. As a future study, initial disturbance manipulation and liquid jet velocity can be studied in order to minimize the formation of satellite droplets.
- More complex fluid mechanic problems can be investigated by means of a high performance parallel computing technique. Therefore, development of current parallel computing abilities of Gerris can significantly assist for further simulations.

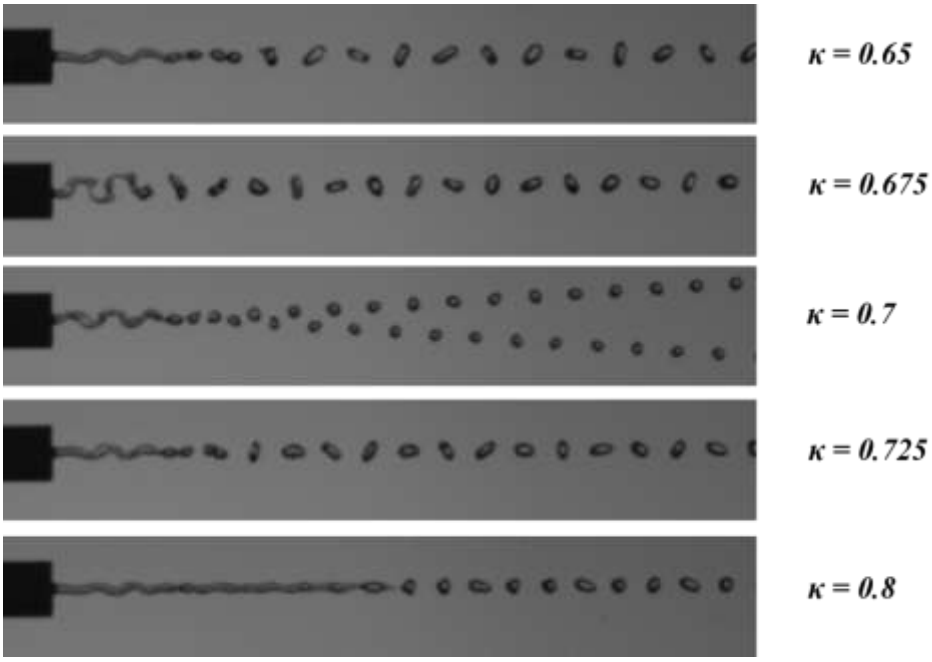

Figure 4-1: Experimental measurements for capillary jet instability with high disturbance amplitude in order of inner diameter of nozzle ($We = 33.47$, and $Re = 872$).

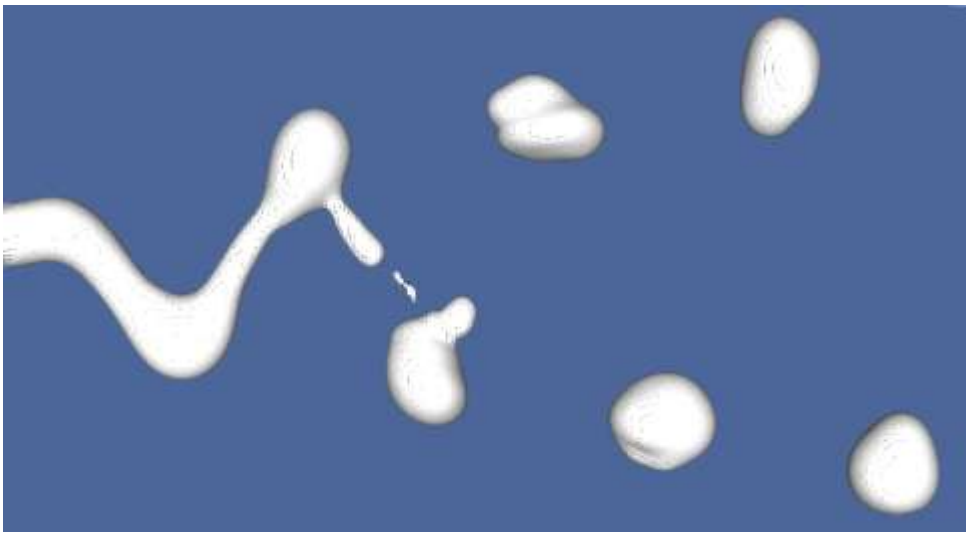

Figure 4-2: Numerical simulation for capillary jet instability with high disturbance amplitude in order of inner diameter of nozzle ($We = 29.6$, and $Re = 840$).

Bibliography

Agbaglah G, Delaux S, Fuster D, Hoepffner J, Josserand C, et al. 2011. Parallel simulation of multiphase flows using octree adaptivity and the volume-of-fluid method. *Comptes Rendus Mec.* 339(2):194–207

Almgren AS, Bell JB, Crutchfield WY. 2000. Approximate projection methods: part i. inviscid analysis. *SIAM J. Sci. Comput.* 22(4):1139–59

Amini G, Ihme M, Dolatabadi A. 2013. Effect of gravity on capillary instability of liquid jets. *Phys. Rev. E*. 87(5):53017

Arai M, Amagai K. 1999. Surface wave transition before breakup on a laminar liquid jet bt - proceedings of the 1998 14th international conference on liquid atomization and spray systems, july 6, 1998 - july 8, 1998. *Int. J. Heat Fluid Flow*. 20(5):507–12

Ashgriz N, Mashayek F. 1995. Temporal analysis of capillary jet breakup. *J. Fluid Mech.* 291:163–90

Ashgriz N, Yarin AL. 2011. Capillary instability of free liquid jets. In *Handbook of Atomization and Sprays*, pp. 3–53. Springer

Bell JB, Colella P, Glaz HM. 1989. A second-order projection method for the incompressible navier-stokes equations. *J. Comput. Phys.* 85(2):257–83

Blaisot JB, Adeline S. 2003. Instabilities on a free falling jet under an internal flow breakup mode regime. *Int. J. Multiph. flow*. 29(4):629–53

Bogy DB. 1979. Drop formation in a circular liquid jet. *Annu. Rev. Fluid Mech.* 11(1):207–28

Bremond N, Clanet C, Villermaux E. 2007. Atomization of undulating liquid sheets. *J. Fluid Mech.* 585:421–56

Cervone A, Manservisi S, Scardovelli R. 2010. Simulation of axisymmetric jets with a finite element navier–stokes solver and a multilevel vof approach. *J. Comput. Phys.* 229(19):6853–73

Cheong BS, Howes T. 2004. Capillary jet instability under the influence of gravity. *Chem. Eng. Sci.* 59(11):2145–57

Chigier N, Reitz RD. 1996. Regimes of jet breakup and breakup mechanisms (physical aspects). . 166:109

Chorin AJ. 1969. On the convergence of discrete approximations to the navier-stokes equations. *Math. Comput.* 23(106):341–53

Cordero ML, Gallaire F, Baroud CN. 2011. Quantitative analysis of the dripping and jetting regimes in co-flowing capillary jets. *Phys. Fluids*. 23:94111

Delteil J, Vincent S, Erriguible A, Subra-Paternault P. 2011. Numerical investigations in rayleigh breakup of round liquid jets with vof methods. *Comput. Fluids*. 50(1):10–23

Dumouchel C. 2008. On the experimental investigation on primary atomization of liquid streams. *Exp. Fluids*. 45(3):371–422

Eggers J, Villermaux E. 2008. Physics of liquid jets. *Reports Prog. Phys.* 71(3):36601

Eroglu H, Chigier N, Farago Z. 1991. Coaxial atomizer liquid intact lengths. *Phys. Fluids A Fluid Dyn.* 3(2):303–8

Erriguible A, Vincent S, Subra-Paternault P. 2012. Simulation of jet disintegration in a supercritical reactor. *Mech. Res. Commun.* 40:52–55

Fuster D, Bague A, Boeck T, Le Moyne L, Leboissetier A, et al. 2009. Simulation of primary atomization with an octree adaptive mesh refinement and vof method. *Int. J. Multiph. Flow*. 35(6):550–65

González H, García FJ. 2009. The measurement of growth rates in capillary jets. *J. Fluid Mech.* 619:179–212

Grant RP, Middleman S. 1966. Newtonian jet stability. *AIChE J.* 12(4):669–78

Hancock MJ, Bush JWM. 2002. Fluid pipes. *J. Fluid Mech.* 466(1):285–304

Heinzl J, Hertz CH. 1985. Ink-jet printing. *Adv. Electron. electron Phys.* 65:91–171

Ibrahim EA, Akpan ET. 1998. Liquid sheet instability. *Acta Mech.* 131(3-4):153–67

Ibrahim EA, Marshall SO. 2000. Instability of a liquid jet of parabolic velocity profile. *Chem. Eng. J.* 76(1):17–21

Jalaal M. 2012. *Direct Numerical Simulation of Fragmentation of Droplets*. University of British Columbia

Jalaal M, Mehravaran K. 2012. Fragmentation of falling liquid droplets in bag breakup mode. *Int. J. Multiph. Flow*. 47:115–32

Kalaaji A, Lopez B, Attane P, Soucemarianadin A. 2003. Breakup length of forced liquid jets. *Phys. Fluids*. 15:2469

Kamphoefner FJ. 1972. Ink jet printing. *Electron Devices, IEEE Trans.* 19(4):584–93

Karasawa T, Tanaka M, Abe K, Shiga S, Kurabayashi T. 1992. Effect of nozzle configuration on the atomization of a steady spray. *At. Sprays*. 2(4):

Leroux S, Dumouchel C, Ledoux M. 1996. The stability curve of newtonian liquid jets. *At. Sprays*. 6(6):

Lin SP, Lian ZW. 1990. Mechanisms of the breakup of liquid jets. *AIAA J.* 28(1):120–26

Lin SP, Reitz RD. 1998. Drop and spray formation from a liquid jet. *Annu. Rev. Fluid Mech.* 30(1):85–105

Lukacs G, Maloney N, Hegner M. 2011. Ink-jet printing: perfect tool for cantilever array sensor preparation for microbial growth detection. *J. Sensors*. 2012:

Malot H, Blaisot J. 2000. Droplet size distribution and sphericity measurements of low-density sprays through image analysis. *Part. Part. Syst. Charact.* 17(4):146–58

Ménard T, Tanguy S, Berlemont a. 2007. Coupling level set/vof/ghost fluid methods: validation and application to 3d simulation of the primary break-up of a liquid jet. *Int. J. Multiph. Flow*. 33(5):510–24

Michalke A, Hermann G. 1982. On the inviscid instability of a circular jet with external flow. *J. Fluid Mech.* 114:343–59

Minemoto T, Okamoto C, Omae S, Murozono M, Takakura H, Hamakawa Y. 2005. Fabrication of spherical silicon solar cells with semi-light-concentration system. *Jpn. J. Appl. Phys.* 44(7R):4820

Montgomery DC. 2008. *Design and analysis of experiments*. John Wiley & Sons

Pan Y, Suga K. 2006. A numerical study on the breakup process of laminar liquid jets into a gas. *Phys. fluids*. 18:52101

Percin G, Khuri-Yakub BT. 2003. Piezoelectric droplet ejector for ink-jet printing of fluids and solid particles. *Rev. Sci. Instrum.* 74(2):1120–27

Plateau J. 1945. Statique experimentale et theorique des liquids soumis aux seules forces moleculaires. cited by lord rayleigh, theory of sound, vol. ii

Popinet S. 2003. Gerris: a tree-based adaptive solver for the incompressible euler equations in complex geometries. *J. Comput. Phys.* 190(2):572–600

Popinet S. 2009. An accurate adaptive solver for surface-tension-driven interfacial flows. *J. Comput. Phys.* 228(16):5838–66

Rayleigh, Lord. 1879. On the capillary phenomena of jets. *Proc. R. Soc. London*. 29(196-199):71–97

Riahi DN. 2009. On spatial instability of electrically forced axisymmetric jets with variable applied field. *Appl. Math. Model.* 33(9):3546–52

Richards JR, Lenhoff AM, Beris AN. 1994. Dynamic breakup of liquid–liquid jets. *Phys. Fluids*. 6:2640

Rohani M, Jabbari F, Dunn-Rankin D. 2010. Breakup control of a liquid jet by disturbance manipulation. *Phys. Fluids*. 22(10):

Sander W, Weigand B. 2008. Direct numerical simulation and analysis of instability enhancing parameters in liquid sheets at moderate reynolds numbers. *Phys. Fluids*. 20(5):

Shimasaki S, Taniguchi S. 2011. Formation of uniformly sized metal droplets from a capillary jet by electromagnetic force. *Appl. Math. Model.* 35(4):1571–80

Sirignano WA. 1993. Fluid dynamics of sprays--1992 freeman scholar lecture. *J. Fluids Eng. States)*. 115(3):

Sirignano WA, Mehring C. 2000. Review of theory of distortion and disintegration of liquid streams. *Prog. Energy Combust. Sci.* 26(4):609–55

Srinivasan V, Salazar AJ, Saito K. 2011. Modeling the disintegration of modulated liquid jets using volume-of-fluid (vof) methodology. *Appl. Math. Model.* 35(8):3710–30

Strutt JW, Rayleigh, Lord. 1879. On the instability of jets. *Tr. Mat. O-va*, pp. 4–13

Sussman M, Puckett EG. 2000. A coupled level set and volume-of-fluid method for computing 3d and axisymmetric incompressible two-phase flows. *J. Comput. Phys.* 162(2):301–37

Taylor GI. 1940. Generation of ripples by wind blowing over a viscous fluid. *Sci. Pap. GI Taylor*. 3:244–54

Tomar G, Fuster D, Zaleski S, Popinet S. 2010. Multiscale simulations of primary atomization. *Comput. Fluids*. 39(10):1864–74

Vu T V., Homma S, Tryggvason G, Wells JC, Takakura H. 2013. Computations of breakup modes in laminar compound liquid jets in a coflowing fluid. *Int. J. Multiph. Flow*. 49:58–69

Weber C, Hutchinson CH, Love WJ. 1948. *On the breakdown of a fluid jet*

Wegener M, Muhmood L, Sun S, Deev A V. 2014. The formation and breakup of molten oxide jets. *Chem. Eng. Sci.* 105:143–54

Yang HQ. 1992. Asymmetric instability of a liquid jet. *Phys. Fluids A Fluid Dyn.* 4(4):681–89

Zhang KKQ, Shotorban B, Minkowycz WJ, Mashayek F. 2010. A comprehensive approach for simulation of capillary jet breakup. *Int. J. Heat Mass Transf.* 53(15):3057–66

Appendix A: Mesh Independency

Simulations are carried out with varied mesh resolutions, refinements 6, 7, and 8. By comparing results, refinement 8 is selected for the numerical study. Figure A-1 illustrates the breakup length to the nozzle diameter ratio for three different mesh refinements. As Figure A-1 shows, L/D variation is quite similar for refinement 7 and 8 while refinement 6 shows different values. In addition t-test is used to check the differences statistically [t-test, $\alpha = 0.05$, $p < 0.05$ for $\mu_1 \neq \mu_2$ (Montgomery 2008)]. Although, the t-test indicates that the breakup length results refinement 6 and 7 (see Table A-1) are significantly different, increase of mesh refinement results to statistically same results for refinement 7 and 8 (see Table A-2). This shows that refinement 7 is enough for the models to be grid independent. In current study, although, refinement 7 is good enough to obtain accurate results and it would be unnecessarily and take more time to run the simulations with refinement 8, the numerical results in section 3 are presented with refinement 8.

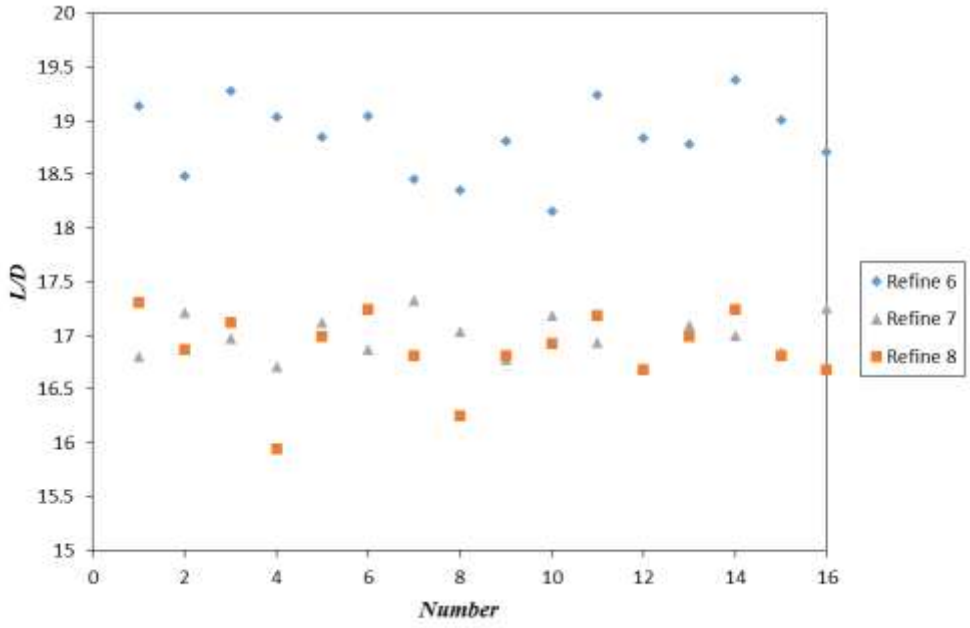

Figure A-1: Breakup length to the nozzle diameter ratio for different mesh refinement to check mesh independency

Table A-1: t-Test, Two-Sample Assuming Unequal Variances for Refinement 6 and 7

	Mesh7	***Mesh6***
Mean	16.988	18.847
Variance	0.039202133	0.12183
Observations	16	16
Hypothesized Mean Difference	0	
df	24	
t Stat	-18.53036641	
P(T<=t) one-tail	5.02365E-16	
t Critical one-tail	1.71088208	
P(T<=t) two-tail	1.00473E-15	
t Critical two-tail	2.063898562	

Table A-2: t-Test, Two-Sample Assuming Unequal Variances for Refinement 7 and 8

	Mesh7	***Mesh8***
Mean	16.988	16.866
Variance	0.039202133	0.13162
Observations	16	16
Hypothesized Mean Difference	0	
df	23	
t Stat	1.180713967	
P(T<=t) one-tail	0.124891526	
t Critical one-tail	1.713871528	
P(T<=t) two-tail	0.249783053	
t Critical two-tail	2.06865761	

In addition, results are presented with different mesh resolutions for reduction of jet radius in the necking zone before jet breakup (See Figure A-2). In the current analysis, the adaptive mesh refinement (AMR) technique is applied in the liquids interface in order to minimize the computational error in this zone instead of entire domain. It is obvious that jet instability behavior is relatively dependent on the mesh size. It is observed that by reducing the mesh

grade size, the accuracy of the results is increased. The difference between the numerical data and theory is significantly high when the mesh in the interface is progressively coarsened (Refinement 6). Again, refinement 7 and 8 represent quite similar results as expected. High mesh refinement which is used in these simulations provides accurate prediction of interface position.

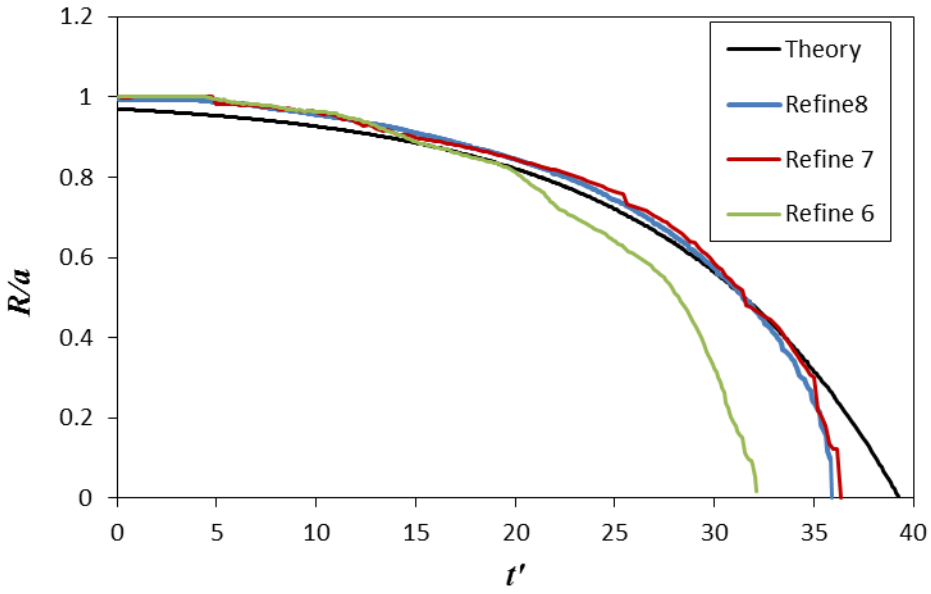

Figure A-2: Numerical simulation for reduction of jet radius in the necking zone before jet breakup with different mesh resolution in comparison with theoretical results from Rayleigh theory ($\kappa = 0.7$ and $\xi_0 = 0.02$)

As shown in Figure A-3, the growth rate was computed for different level of refinement. The continuous line indicated the dispersion relation from linear instability analysis from Rayleigh theory. Comparison between numerical results by VOF method and theoretical ones shows that, at the fine mesh sizes (Refinement 7 and 8), the growth rate is not sensitive to the refinement level although at low resolution (refinement 6) the difference between numerical results and theoretical prediction increases. Results for instability growth indicate when finer

meshes exist at the interface; the numerical results show better agreement with theoretical prediction.

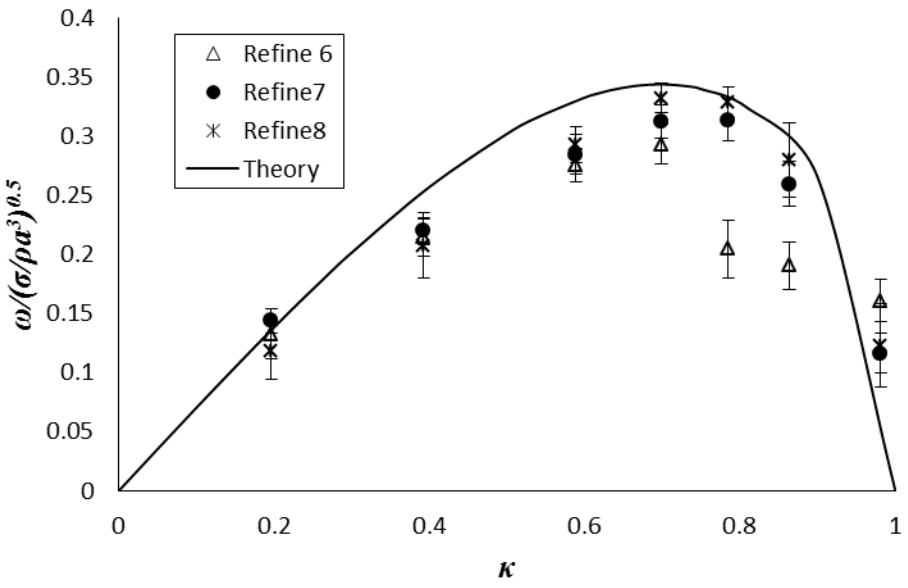

Figure A-3: Numerical and theoretical non-dimensional growth rate versus wave number with initial disturbance, $\xi_0 = 0.04$, $We = 29.6$, and $Re = 840$.